

Naval Research Laboratory

Washington, DC 20375-5320



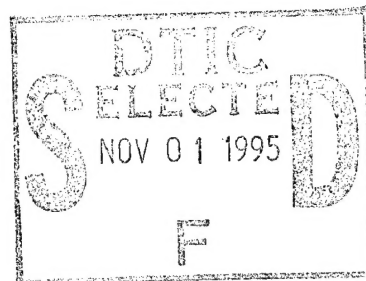
NRL/MR/6756--95-7734

Nonlinear Particle Dynamics in the Magnetotail: A Laboratory Study

1. The Experimental Configuration and Numerical Simulation

D. WALKER
J. CHEN
C. SIEFRING
D. DUNCAN
J. STRACKA
J. ANTONIADES

*Charged Particle Physics Branch
Plasma Physics Division*



J. BOWLES

*SFA, Inc.
Landover, MD*

Original contains color plates: All DTIC reproductions will be in black and white

D. HOLLAND

*Physics Department
Illinois State University*

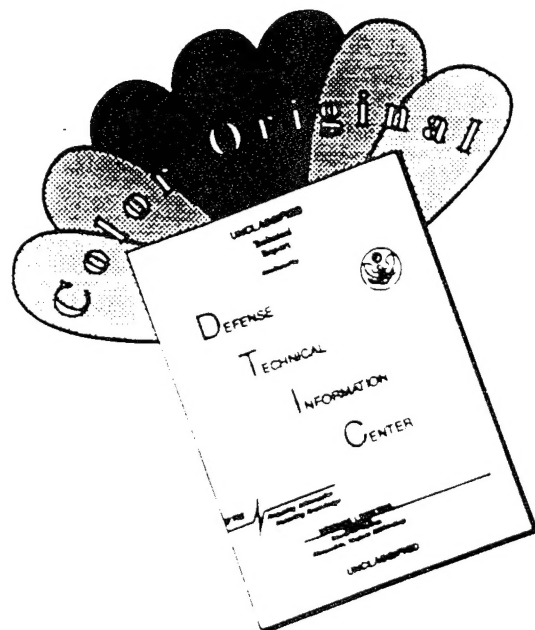
19951030 124

September 25, 1995

DTIC STAMP AND APPROVAL FIELD

Approved for public release; distribution unlimited.

DISCLAIMER NOTICE



**THIS DOCUMENT IS BEST
QUALITY AVAILABLE. THE COPY
FURNISHED TO DTIC CONTAINED
A SIGNIFICANT NUMBER OF
COLOR PAGES WHICH DO NOT
REPRODUCE LEGIBLY ON BLACK
AND WHITE MICROFICHE.**

REPORT DOCUMENTATION PAGE

*Form Approved
OMB No. 0704-0188*

Public reporting burden for this collection of information is estimated to average 1 hour per response, including the time for reviewing instructions, searching existing data sources, gathering and maintaining the data needed, and completing and reviewing the collection of information. Send comments regarding this burden estimate or any other aspect of this collection of information, including suggestions for reducing this burden, to Washington Headquarters Services, Directorate for Information Operations and Reports, 1215 Jefferson Davis Highway, Suite 1204, Arlington, VA 22202-4302, and to the Office of Management and Budget, Paperwork Reduction Project (0704-0188), Washington, DC 20503.

1. AGENCY USE ONLY (Leave Blank)			2. REPORT DATE		3. REPORT TYPE AND DATES COVERED	
			September 25, 1995		Interim	
4. TITLE AND SUBTITLE Nonlinear Particle Dynamics in the Magnetotail: A Laboratory Study 1. The Experimental Configuration and Numerical Simulation					5. FUNDING NUMBERS	
6. AUTHOR(S) D. Walker, J. Bowles,* D. Holland,** J. Chen, C. Siefring, D. Duncan, J. Stracka, and J. Antoniades						
7. PERFORMING ORGANIZATION NAME(S) AND ADDRESS(ES) Naval Research Laboratory Washington, DC 20375-5320					8. PERFORMING ORGANIZATION REPORT NUMBER NRL/MR/6756-95-7734	
9. SPONSORING/MONITORING AGENCY NAME(S) AND ADDRESS(ES) Office of Naval Research 800 North Quincy Street Arlington, VA 22217-5660					10. SPONSORING/MONITORING AGENCY REPORT NUMBER	
11. SUPPLEMENTARY NOTES *SFA, Inc., Landover, MD **Physics Department, Illinois State University						
12a. DISTRIBUTION/AVAILABILITY STATEMENT Approved for public release; distribution unlimited.					12b. DISTRIBUTION CODE	
13. ABSTRACT (Maximum 200 words) We have performed the initial stages of an experiment designed to investigate particle dynamics in the magnetotail. The experiment was developed for and performed in the large Space Physics Simulation Chamber (SPSC) at the Naval Research Laboratory. The results of this experiment lend support to the idea that particle scattering from the magnetotail neutral sheet is not random but that there exist resonances in the number and direction of scattered particles as a function of energy. The effort began with construction and testing of the magnetic field configuration necessary to simulate the quite-time magnetotail field: a neutral sheet magnetic field profile $B_0(z)x$ with a superimposed normal field B_zz . Once complete, electrons of variable energy were injected into the field region created and the scattered current collected by back-scattered and forward-scattered collection plates was analyzed as a function of electron energy. The experiment was used to test the hypothesis that single particle scattering from a neutral sheet type profile as described can be "coherent" and can at times demonstrate resonance effects as a function of energy.						
14. SUBJECT TERMS Magnetotail Particle Experiment					15. NUMBER OF PAGES 70	
					16. PRICE CODE	
17. SECURITY CLASSIFICATION OF REPORT UNCLASSIFIED	18. SECURITY CLASSIFICATION OF THIS PAGE UNCLASSIFIED	19. SECURITY CLASSIFICATION OF ABSTRACT UNCLASSIFIED	20. LIMITATION OF ABSTRACT UL			

TABLE OF CONTENTS

Section	Page
ABSTRACT.....	1
I Introduction.....	1
I.1 Theory.....	2
I.2 Experiment.....	4
II Approach.....	4
II.1 Experimental Design.....	4
II.2 Description of Particle Code.....	5
II.3 Finite Wire Effects.....	7
II.4 Effects of Finite Grid Size.....	7
III Overall Objectives.....	10
IV Experimental Configuration.....	10
IV.1 Experimental Chamber Description.....	10
IV.2 Mechanical Design Considerations.....	11
IV.2.1 Grid Design.....	11
IV.2.2 B(dot) Loop Probe.....	12
IV.2.3 Current Collector Plates.....	12
IV.2.4 Pulse Forming Network.....	13
IV.2.5 Electron Beam.....	13
V Experimental Results.....	13
V.1 Current Collection during Pulsing.....	13
V.2 Magnetic Field.....	14
VI Comparison of Results to Theory.....	15
VI.1 Theoretical Resonance Dependence of bn.....	15
VI.2 Simple Theory.....	16
VI.3 Results from Numerical Work.....	18
VI.4 Experimental Results.....	18
VI.4.1 Resonances.....	19
VI.4.2 Collected Current as a function of y.....	20
VII Scaling Considerations and Future Work.....	20
VIII References.....	22

For	
DRA&I	<input checked="" type="checkbox"/>
FAB	<input type="checkbox"/>
Planned	
ion	
on /	
Availability Codes	
Dist	Avail and / or Special
A-1	

Nonlinear Particle Dynamics in the Magnetotail: A Laboratory Study

1. The Experimental Configuration and Numerical Simulation

DN Walker, J. Bowles^a, D. Holland^b, J. Chen, C. Siefring, D. Duncan^a, J. Stracka
and J. Antoniades

^aSachs Freeman Assoc., Landover MD, ^bPhysics Dept., Illinois State University

ABSTRACT

We have performed the initial stages of an experiment designed to investigate particle dynamics in the magnetotail. The experiment was developed for and performed in the large Space Physics Simulation Chamber (SPSC) at the Naval Research Laboratory. The results of this experiment lend support to the idea that particle scattering from the magnetotail neutral sheet is not random but that there exist resonances in the number and direction of scattered particles as a function of energy. The effort began with construction and testing of the magnetic field configuration necessary to simulate the quiet-time magnetotail field: a neutral sheet magnetic field profile $B_0(z)$ with a superimposed normal field B_z . Once complete, electrons of variable energy were injected into the field region created and the scattered current collected by back-scattered and forward-scattered collection plates was analyzed as a function of electron energy. The design of the particle detector plates for back- and forward-scattered collection, along with noise shielding, secondary emission suppression and testing to insure that the electron beam represented single particle behaviour were key elements in the experimental buildup phase. In addition theoretical modelling of the experimental configuration was a primary contributor to the basic feasibility study and ultimate design of the effort. The experiment was used to test the hypothesis that single particle scattering from a neutral sheet type profile as described can be "coherent" and can at times demonstrate resonance effects as a function of energy. The final experimental configuration was not a perfect realization of the idealized Harris magnetic field form but retained important features necessary for resonance structures as predicted by the design software. This paper, which is concerned with a description of the design and ultimate experimental build-up for the effort, is the first of two papers. The second paper concentrates primarily on the initial results of the experimentation and will follow shortly as a companion paper.

I Introduction

This paper documents the design and buildup of an unusual laboratory experiment designed to examine recent theoretical predictions of nonlinear particle dynamics in a magnetic field which is designed to simulate the earth's magnetotail, the modified Harris field. As the magnetotail is believed to be important for energy storage and release, the structure of the tail, including the current sheet, is a key element necessary for understanding large scale changes in the magnetic field, particle acceleration and other physical effects associated with geomagnetic substorms. The global structure, however, is difficult to ascertain as there is as yet no "snapshot" of the magnetosphere available. On the other hand, particle distribution functions are directly accessible via in-situ measurements and there have been attempts to deduce global attributes of the magnetosphere from point measurements of plasmas. Also, since charged particle motion is governed by the large-scale magnetic and electric fields, information related to global

thorough analysis of the particle dynamics. As a result, the nonlinear dynamics of charged particles moving in these fields continues as an integral part of a complete characterization of the magnetosphere.

The laboratory experiment is designed to provide a surrogate global system which has the topological properties of the magnetotail. Because distribution functions and current sheet structure are related to the phase space structure of the magnetic configuration, we have numerically investigated particle motion in experimentally realizable fields. Initially we have investigated coherence scattering properties in the different fields and ultimately we intend to construct pitch-angle resolved distribution functions in the field to accompany those predicted by the numerical simulations. These efforts have led to the experimental configuration of four current carrying meshes described below. Finally, we have related the computed distribution functions to the scale length of the mesh-generated field. In these numerical calculations, various important realistic experimental constraints have been included. For example, the finite mesh wire thickness and the attendant field inhomogeneities, in addition to the deviation of the field from the Harris form have been included explicitly as outlined below.

I.1 Theory

There has been considerable effort over the years in understanding magnetotail charged particle motion in the attempt to explain various properties of this near earth region. The quiet time magnetotail magnetic field may be modelled by a neutral sheet profile $B_0(z)\hat{x}$ with a superimposed normal field $B_z\hat{z}$ where \hat{x} and \hat{z} are unit vectors: the so-called "quasi-neutral sheet" geometry. Figure (1) is a model magnetic field which has the general topology of the magnetotail field depicted in Figure (2). The coordinate system is also shown in Figure (1). The sunward direction is along the positive x-axis. A considerable volume of early work already exists which deals with a number of specialized aspects of the particle motion. The methods used include approximate analytical methods [Speiser, 1965; Alekseyev and Kropotkin, 1970; Sonnerup, 1971; Stern and Palmadesso, 1975; Pellat and Schmidt, 1979] and numerical methods [Speiser, 1967; Cowley, 1971; Eastwood, 1972; Swift, 1977; Speiser and Lyons, 1984]. West et al.[1978a,b] and Wagner et al.[1979] studied orbits that are now known as stochastic orbits.

In all of the works cited above the underlying implicit concept is that particle motion in a quasi-neutral sheet is ultimately regular and integrable. Chen and Palmadesso, [1986] were able to show that particle motion in the quasi-neutral sheet (modified Harris magnetic field form) is nonintegrable with only two constants of the motion, and that the phase space is partitioned into disjoint regions occupied by dynamically distinct classes of orbits which they characterize as stochastic, integrable (regular) and transient. Examples of these phase space plots are shown in Figure (3). There are visible in the plots, discrete regions or distinct boundaries which have been shown to isolate incoming particles (entry) from outgoing ones (exit). The two constants of the motion which are sufficient to parameterize the particle motion are a normalized Hamiltonian, \tilde{H} and a parameter related to the magnetic field topology, $b_n = B_z/B_{x0}$. Considerable attention has been given also by other authors to understanding the nature of the nonintegrable motion in the magnetotail [Buechner and Zelenyi, 1986, 1989; Kaufmann et al., 1993(a), 1993(b); Kaufmann and Lu, 1993]. For example, Buechner and Zelenyi [1989] have similarly derived a parameter κ related to the normalized Hamiltonian ($\kappa = (2\tilde{H})^{1/4}$) which they use as a measure of chaos: for $\kappa \sim 1$ chaos is greatest and is reduced for $\kappa \ll 1$ and for $\kappa \gg 1$. For purposes here, chaotic behaviour really means that the final states, after interaction with a scattering center, have a sensitive dependence on the initial states, i.e., if all orbits were truly only stochastic there would be no relationship between these two asymptotic states whatsoever. The physical implications of particle orbits in the magnetotail including stochastic orbits have been treated by numerous authors [Chen et al., 1990a,b; Doxas et al., 1990; Horton and Tajima, 1990; Burkhardt and Chen, 1991; Ashour-Abdalla et al., 1990].

The entry and exit subregion boundaries defined above are important because these regions define the measurable states of particle trajectories and are connected to the asymptotic regions via these trajectories. A satellite measurement of particles, for example, samples asymptotic, or final state, properties of the particles. Also, initial and final pitch angles are characterized as incoming and outgoing. The stochastic, transient and integrable particle orbits occupy different and distinct regions of phase space delineated by the boundaries discussed above and the classes of orbits allowed are characterized by widely different time scales. It was suggested that the phase space partition and the separation of time scales can lead to non-Maxwellian features in the distribution functions in response to changes in boundary conditions, i.e., in the asymptotic distribution. It was shown that at certain energies given approximately by $\hat{H}^{1/4} = N + 0.6$, particles approaching the midplane from the asymptotic region have limited access to the stochastic regions; conversely, particles that are in the stochastic regions at the resonance energies are trapped near the midplane for long periods of time. Put another way, at these energies the particles have transient characteristics and therefore after being injected can be measured as they emerge on more or less the same time scale. These ideas lead to the concepts of differential memory and "coherent" scattering. Using the model field of Figure (1), Burkhardt and Chen, [1991] modelled the CPS distributions and in particular introduced a density change in the initial distribution at $t=0$. The subsequent time evolution of the distribution function $f(v,t)$ is calculated for $t > 0$. The results show that, following such a change, the distribution function $f(v)$ develops measurable peaks and valleys whose locations obey the characteristic scaling law of $\hat{H}^{1/4}$. Here \hat{H} is the normalized Hamiltonian for each species and is defined by $\hat{H} = (mv^2/2)/(mb_n \Omega_n^2 \delta^2)$ where $b_n = B_{z0}/B_{x0}$ and $\Omega_n = eB_{z0}/mc$. The resonance scaling then is given by $N + .06 \sim \hat{H}^{1/4}$ where N represents integers. A plot of the model steady state distribution function at $z = +3\delta$ is shown in Figure (5) as an illustration of the resonance effect found above. We explore this figure and its relationship to Figure (4) in more detail below.

The effects of collisions on the phase space orbits are of interest because the physical properties above have been deduced from these orbits in the absence of particle scattering. For example, the scaling law above, which has been predicted for the location of peaks and valleys in ion distribution functions in the central plasma sheet [Burkhardt and Chen, 1991] should be re-examined in the presence of collisions for possible important effects on physical properties. This has been investigated in numerical simulations in relation to pitch-angle scattering and energy exchange [Holland and Chen, 1991], but as yet no laboratory work has been undertaken. Moreover, the non-Maxwellian distribution function with a resonance scaling $N \sim \hat{H}^{1/4}$ shows very good agreement with observations [Chen et al., 1990a] and has been shown to be unstable to electrostatic waves [Huba et al., 1991].

An important conclusion from above is that analysis of particle motion predicts that the phase space particle orbits are separable into the distinct stochastic, transient and integrable regions. Each class of orbit is dynamically distinct and, as seen in Figure (3), even the regions are disjoint from one another. The time scales associated with each of these regions can be used to define separate classes of particles. For example, the resonance scaling given above was originally derived in connection with the "transient regions" in the phase space and, as is pointed out by [Burkhardt and Chen, 1991], the "stochastic regions" seen in Figure (3) constitute an altogether separate class of particles and do not overlap the resonant energy regions. At the N -th such resonance, the majority of the transient particles crosses the equator $N + 1$ times. If $N + 1$ is even (odd), such orbits originating from $z = \infty$ will enter the equatorial plane and escape to $z = +\infty(-\infty)$. Viewed as a chaotic scattering system, therefore, the current sheet scatters the transient particle class "coherently" at resonance. In Figure (4), we have plotted $C_r = 1 - R$ versus $\hat{H}^{1/4}$ for a particular choice of b_n . Here $R = n/s(n < s)$ or $R = s/n(s < n)$ where n and s are the fraction of north ($z > 0$)- or south-bound scattered orbits, respectively, relative to the incoming orbits from $z = +\infty$ with normalization $n + s = 1$.

As an illustration, we show in Figure (5) a model distribution function $f(v)$ using C_r of Figure (4)

based on the above model. The observer is assumed to be at $z = +3\delta$. Maxwellians $f_j = \exp(-HT_j)$ ($j = 1, 2$) are used for the source distributions with $f_2(0) = \beta f_1(0)$. For this figure, we have used $T_1 = 20000$ °K, $T_2 = 16000$ °K, $\beta = .5$ and $b_n = 0.05$. f_1 represents particles scattered toward the current sheet from the North and f_2 from the South. No attempt to fit a specific data set is made.

I.2 Experiment

It has been pointed out a number of times that space-related laboratory experimentation can be divided into at least two separate categories (e.g., Faelthammar, 1974): (i) experiments intended to investigate basic physical processes which play a role in space plasma dynamics, and (ii) experiments designed to literally simulate geophysical structures. When considering experimentation related to the second category, scaling considerations become paramount and can be so stringent as to put into question the applicability of the results to space physics [Block, 1967; Fahleson, 1967]. Laboratory work of this nature, for example the early terella series of experiments, has met with limited, but at times, impressive success [Block, 1955, 1956; Alfvén et al., 1963, 1964; Kawashima, et al., 1965]. A compilation of the early experiments has been given by Schindler [1969]. A number of other more recent experiments belonging largely to the first category have yielded significant new insight into areas such as magnetic reconnection [Stenzel and Gekelman, 1981] and double layer simulation [Alport et al., 1986; Hairapetian and Stenzel, 1990] and velocity shear instabilities related to the space plasma environment [Koepke and Amatucci, 1994] and parameter regime.

The phenomenon which we investigate here belongs to the class of basic physics of particle dynamics in a magnetosphere-earth magnetic field region. To do this the essential features of the quiet-time magnetotail magnetic field region have been constructed. Our initial purpose is to determine if resonances predicted by the theory can be measured experimentally. The experimental arrangement in the SPSC is shown in schematic form in Figure (6). After constructing an approximation to the magnetotail magnetic field topology using a pulsed grid network, we injected electrons into the "neutral sheet" taking care that the electron beam was sufficiently single particle-like. To investigate whether "coherent" particle scattering occurs at neutral sheet crossings for particular "resonant" particles, we placed detectors (sectored current collection sheets) as shown in Figure (6), varied the energy of the incoming beam, and tracked the number of forward and backscattered particles for a given initial energy; by varying the energy of the injected particles over a wider range we will eventually be able to determine the distribution.

II Approach

The theoretical basis of this study is sketched in the Introduction and the major references are given therein. This Section focusses on the experimental method and its relationship to the particle code which was used to define parameter ranges and which also was essential in predicting which of the physical models under consideration would provide the basic resonance structures discussed above.

II.1 Experimental Design and Configuration

In developing the experimental field model and configuration we have used a test particle simulation as described in the following Section II.2. This simulation allowed us to vary the value of b_n , the number and

simulation as described in the following Section II.2. This simulation allowed us to vary the value of b_n , the number and location of the current sheets, as well as the current carried by each sheet. In addition, the model includes both the discrete nature of the wires and their finite radius. With these inclusions, we were able to determine the amount of scattering as particles cross the sheet and the percentage of particles which are lost.

In preparing the laboratory experiments we chose to model the distributed neutral sheet using a number of equally spaced thin current sheet sections. Such a series of distributed transmissive current sheets approximates the Harris magnetic field form. The thin current sheets were constructed using highly transparent arrays of wires as shown schematically in Figure (7). In theory, by using an arbitrarily large number of properly weighted thin sheets, we could reproduce the true Harris current distribution. In practice, however, it is desirable to use the minimum number of sheets possible since for each crossing of a sheet there is a finite probability of losing the particle. In addition, the discrete nature of the grid wires causes a small amount of scattering. Computer simulations, as covered in Section II.2 below, using varying numbers of grids have shown that the optimum representation consists of four grids as pictured (the "quadgrid" model). Also simulations show that finite wire effects are negligible for wire sizes selected.

The choice of $1\text{m} \times 1\text{m}$ grids is a compromise between the desire to maintain field constancy and size constraints imposed by the chamber environment. Because of the finite size along the y-direction, the desire for field constancy requires a relatively small separation between adjacent sheets. This allows a measurement of the most number of resonant peaks for a given b_n . In addition, it is necessary to separate the wires as much as possible without disturbing field constancy around a particular wire to reduce scattering and particle losses. From an experimental viewpoint, however, it is desirable to have the wires as large as possible (to carry more current). In the simulations we have used wires ranging from 40 to 80 microns and in the laboratory we have tested the current carrying capability of tungsten and other materials from 10 to 70 microns. We have used wire separations ranging from 1mm to 2mm, sheet separations from 1 to 5 cm and b_n ranging from 0.1 to 0.4 in the test particle simulations. We found that the experimental configuration which best met the conflicting requirements was a four sheet configuration of 1.8 cm separation between planes, an inter-wire spacing of 1.59 mm, a wire radius of 60 microns and a normalized magnetic field ratio, b_n , of 0.2. In this arrangement, 60% of the current is carried by the two inner sheets with the remaining 40% carried by the two outer sheets. Also there are current carrying field shaping bars pictured in Figure (8) which carry currents of the same order of magnitude as the entire sheet (see below).

For the configuration defined above we find that at the very low energies particle loss is 50% of electrons in traversing the structure, whereas at the higher energies this figure is 10%. Our experimentation only used particle energies greater than about 200 eV with most experimentation in the 100's of eV to keV range. As described below, in many cases of interest low entry particle pitch angles were maintained thus allowing higher energies in examining the resonance effects. We did not expect any significant effects on the scattering amplitudes due to particle interaction with the wires and this is confirmed by experimentation results. Very low energy particles (in the eV to 10's of eV range) experience unacceptable levels of scattering in addition to being affected much more by noise levels apparent in any pulsed environment such as the one described here. Also, for wire radii which are larger, we began to lose an unacceptably large percentage of the particles and therefore the resonance structures lose resolution. We describe the effects of finite wire sizes below.

II.2 Description of particle code

The theoretical modeling of the experiment was performed using a test particle code in which a source distribution of particles is selected and pushed through a prescribed magnetic field. The numerical algorithm used is the standard leap frog method with the step size chosen small enough to resolve the highest frequency (shortest scale length) in the system.

We have written the code so that we may use a number of model input distribution functions. In particular, for any given energy (or multiple energies) we launch N particles with a random spread in pitch and phase angle (δ, ϕ) about a given pitch angle β and phase angle θ . Note that by choosing β , θ and $\delta\phi$ we may model anything from beams to completely isotropic distributions.

The models used for magnetic field went through a number of iterations listed below. In order to construct a magnetic field with the same general topology as the Earth's magnetotail, (i.e. a long scale length in both the x and y directions and a short scale length in z , where x is the direction of the primary component of the field above the current sheet, y is the direction of the current, and z is normal to the current sheet) we need to have a current sheet which is very broad in both x and y and has a finite thickness in z . Ideally, we would have an infinite current sheet with a current density given by

$$J(z) = J_0 \operatorname{sech}^2(z) \hat{y} \quad (1)$$

(Note that we are using dimensionless variables so the z is normalized to some scale length, L , typically the half-width of the current sheet.) Since this is not possible in a laboratory environment we need to design a surrogate system which has the same general topology as the actual system. We have chosen to use a set of thin current sheets evenly spaced in z with the currents in each grid weighted to mimic the actual distributed current sheet. As a lowest order approximation, we neglect any finite wire effects and take the current sheets to have an infinite extent in both x and y , i.e. we take the current density to be

$$J(z) = J_0 \sum_i \alpha_i \delta(\operatorname{abs}[z - z_i]) \hat{y} \quad (2)$$

where α_i is the fraction of the total current in the i^{th} wire and z_i is its location. Obviously if we use an infinite number of such current sheets we may reconstruct the current density profile of Equation (1) to arbitrary accuracy. In practice, this current distribution must be constructed in the lab using a set of wire grids, and even though these grids are highly transparent, each time a particle passes through one there is a small probability the particle will be absorbed and also a small amount of scattering. Thus, it is desirable to use as small a number of grids as is possible to obtain the desirable results. We have found the minimum number of grids required to obtain the resonance scaling in the forward (backward) scattering probability is four, and that even numbers of grids in general give better results than odd numbers. In particular, we have found that a reasonable model uses four grids with 30% of the total current carried on each of the inner two grids and 20% carried on each of the outer two grids. The inner grids are located at $z = \pm 0.33$ and the outer grids at $z = \pm 1$. This configuration mimics the topology of the magnetotail current sheet quite well for high energy particles which traverse a large fraction of the current sheet thickness in their meandering and therefore tend to integrate over the discrete nature of the grid structure. For low energy particles, on the other hand the quantized nature of the field is quite apparent and the $H^{1/4}$ scaling in the forward (backward) scattering probability is lost.

II.3 Finite Wire Effects

The current sheets in an experimental configuration are not infinitely thin and uniform but are instead constructed from discrete wires which may both scatter and absorb particles. Far from a given current sheet we may neglect the discrete nature of the wires and use the uniform thin sheet approximation. Within a certain distance of a current sheet, however, a particle will "see" the current sheet as being constructed from individual wires. To model this effect, when a particle is within a distance of two wire spacings from a current sheet we model that particular grid as fifty individual wire (± 25 wires in either direction from the location of the particle). The other grids are still modeled as uniform thin sheets, since the particle is far from them. No significant differences were found when a larger number of wires were used. In addition, to account for particles being lost to the grid, if a particle comes within a wire radius of the location of a wire we remove the particle from the simulation. A particularly interesting aspect of the results of this portion of the theoretical modeling is that three grids have a higher transparency (absorbed fewer particles) than would be expected from purely geometrical arguments. This is because the magnetic field near a wire increases as $1/r$ and tends to keep particles from reaching the wire.

II.4 Effects of Finite Grid Size

The next major complication to the ideal case of four infinite, uniform thin grids to be examined is the fact that the grids are not infinite in extent but rather are finite in both x and y . As long as we are within grids, the effects of truncating in the y -direction is not important, however, we find that the truncation in the x -direction results in a significant deviation from a simple field reversal topology. We again neglect the finite wire effects and model each of the grids shown in Figure (8) as a thin current sheet that has a width $2a$. The magnetic field for a current sheet of this form is given by

$$B_x = \frac{\mu_0 I}{4\pi a} \left[\tan^{-1}\left(a - \frac{x}{z}\right) + \tan^{-1}\left(a + \frac{x}{z}\right) \right] \quad (3)$$

and,

$$B_z = \frac{\mu_0 I}{8\pi a} \ln \left[\frac{(a-x)^2 + z^2}{(a+x)^2 + z^2} \right] \quad (4)$$

The total magnetic field from all four grids is found by adding magnetic fields of this form with the appropriate shift in the z for each grid. A vector plot of this field combined with a constant z -component (due to the Helmholtz coils) is plotted in Figure (9). Note that instead of the magnetotail like geometry that we are attempting to reproduce, we have created closed field lines which are much more reminiscent of a O-type geometry.

To rectify this problem we have added shaping bars modeled as current filaments in x -direction of length $2a$ located at either edge of the grids seen in Figure (8). The current being fed into the wire at one end and being bled off is a linear function of x . The feeder bar for the inner two grids is modeled as a single filament located at $z = 0$ and $y = a$, whereas the bar feeding the outer two grids is modeled as two current filaments located at $z = \pm c$ and $y = b$. The currents are fed into the inner and outer grids from opposite ends of the grid. We have calculated the total magnetic field (4 finite grids + shaping bars

+ feeding bars) in this case to be given by

$$B_x = \frac{\mu_0 I}{4\pi a} \left[\frac{\epsilon_0}{2} [Q(a, 1, x, z) + Q(a, -1, x, z)] + \frac{\epsilon_i}{2} [Q(a, 1/3, x, z) + Q(a, -1/3, x, z)] \right. \\ \left. + 2\epsilon_R R(a, a_R, x, z) + 2\epsilon_L R(a, -a_L, x, z) \right] \quad (5)$$

$$B_y = \frac{\mu_0 I}{4\pi a} \left[\frac{\epsilon_i}{2} [G(a, a, 0, x, y, z) - G(a, -a, 0, x, y, z)] - \frac{\epsilon_0}{2} [G(a, b, c, -x, y, z) \right. \\ \left. + G(a, b, -c, -x, y, z) - G(a, -b, c, -x, y, z) - G(a, -b, -c, -x, y, z)] \right] \quad (6)$$

and,

$$B_z = \left[\frac{\epsilon_i}{2} [P(a, 1/3, x, z) + P(a, -1/3, x, z) - H(a, a, 0, x, y, z) + H(a, -a, 0, x, y, z)] \right. \\ \left. + [P(a, 1, x, z) + P(a, -1, x, z) + \frac{1}{2} H(a, b, c, -x, y, z) + \frac{1}{2} H(a, b, -c, -x, y, z) \right. \\ \left. - \frac{1}{2} H(a, -b, c, -x, y, z) + \frac{1}{2} H(a, b, -c, -x, y, z)] \right. \\ \left. - 2\epsilon_R S(a, a_R, x, z) - 2\epsilon_L S(a, -a_L, x, z)] + B_H \right] \quad (7)$$

where the functions G,H,P,Q,R and S are defined as,

$$G(a, b, c, x, y, z) = \frac{z-c}{(z-c)^2 + (y-b)^2} \left[\frac{(x^2-a^2)+(y-b)^2+(z-c)^2}{\sqrt{(a+x)^2+(y-b)^2+(z-c)^2}} - \sqrt{(a-x)^2+(y-b)^2+(z-c)^2} \right] \quad (8)$$

$$H(a, b, c, x, y, z) = \frac{-(y-b)}{(z-c)^2 + (y-b)^2} \left[\frac{(x^2-a^2)+(y-b)^2+(z-c)^2}{\sqrt{(a+x)^2+(y-b)^2+(z-c)^2}} - \sqrt{(a-x)^2+(y-b)^2+(z-c)^2} \right] \quad (9)$$

$$P(a, b, x, z) = \frac{1}{2} \ln \left[\frac{(a-x)^2 + (z-b)^2}{(a+x)^2 + (z-b)^2} \right] \quad (10)$$

$$Q(a, b, x, z) = \tan^{-1} \left(\frac{a-x}{z-b} \right) + \tan^{-1} \left(\frac{a+x}{z-b} \right) \quad (11)$$

$$R(a,b,x,z) = \frac{az}{(x-b)^2 + z^2}, \quad S(a,b,x,z) = \frac{a(x-b)}{(x-b)^2 + z^2} \quad (12)$$

This field is plotted in Figure (10) and it shows similarity to the Harris type model configuration shape to a greater degree than the O-type geometry seen in Figure (9).

We have plotted in Figures (11) through (15) the results of test particle simulations using the final model covered above. We use here and in the majority of the remaining plots the convention that the normalized energy is plotted as $\hat{H}_D^{1/4} = b_n \hat{H}^{1/4}$ as in, for example, Holland and Chen, [1993]. The usefulness of this is evident, as the plots are now not restricted to a particular value of b_n . The conventional values of $\hat{H}^{1/4}$ are then easily recovered simply by dividing abscissa values by b_n . Figure (11) is a plot of the correlation function, C_r , for the case in which $B_0 = 20$ gauss and $\delta = 10$ cm. The resonant peak structures at particular normalized energies are evident in this plot. Figures (12) and (13) are plots of the percentage of particles forward and backward scattered from the four grid region for these parameters. Figures (14) and (15) plotted for this simulated case show a contour plot of scattering amplitudes versus pitch angle with the right hand limit corresponding to forward scattered particles. The resonance peaks are clearly visible in Figure (14) and even more dramatically in the three dimensional view of Figure (15). The source particle distribution for these results represents particles injected within 10 degrees of field alignment. Based on these results we can prepare Table I, for example, which gives electron energy and drift in the y direction for each individual peak. The energies used in the table are beam energies in eV required to resolve the Nth peak for the scale length δ and the given B_x, b_n . The energies are calculated from their normalized values, \hat{H} , by

$$H = \hat{H}(m\Omega_n^2 \delta^2 b_n^2), \quad \hat{H} = (N+0.6)^4 \quad (13)$$

We might note that the magnitude of B_x , the x-component of the field, is chosen here as 20 gauss whereas the z-magnitude is 2 gauss. Also, the resonance peaks are strongest for $\rho_o < R_c$ and the peaks vanish for $\rho_o > R_c$, where R_c is the radius of curvature of field lines in the current sheet.

TABLE 1

Energies to resolve the N th Peak in the distribution function and the distance moved along y (dy)

$B_x = 20$ gauss, $B_z = 2$ gauss, $\delta = 10$ cm

N	E(eV)	dy(cm)
2	32	8
3	120	16
4	340	27
5	800	40
6	1700	62
7	3360	81

The value of δ , which is the half width of the field, is taken here as 10 cm in order to account for the nonlinearity in the region of the wires. It defines the magnetic field and adjustments which must be made to reproduce a given configuration i.e., the shaping of the field and the placement of current carrying conductors is determined by this parameter.

III Overall Objectives

As described previously, we have performed a number of simulation studies of various types of neutral sheet configurations. These results along with earlier models have been used to design the current experimental arrangement. The overall general objectives of the investigation are summarized as follows:

(i) To test the hypothesis that particles injected from the asymptotic regions as described above follow an energy scaling law related to the location of peaks and valleys in the absence of scattering for a vacuum field as shown in Figure (5), (ii) To test the theoretical results that produce the different classes of phase space orbits as seen in Figure (3) i.e., to verify that quiet-time magnetotail distributions can be grouped according to transient, stochastic and integrable regions, (iii) To verify and give a diagnostic for measurement of current sheet thickness based on the energy scaling considerations above and finally, (iv) To introduce noise (i.e., in the form of a variable plasma density) in order to determine the effect on the phase space orbits and the results of the above investigations.

Specific primary experimental questions which we have addressed to date are:

(i) What percentage of injected particles are forward-scattered and back-scattered? (ii) How far across the "neutral sheet" do the particles move? (Our test particle simulations have also predicted these results.) and, (iii) How many crossings are observed at a given energy? i.e., what is N?

IV Experimental Configuration

IV.1 Experimental Chamber Description

The experimental work was performed in the large Space Physics Simulation Chamber (SPSC) at the Naval Research Laboratory as shown schematically in Figure (6). The axial magnetic field provided by the five coil Helmholtz arrangement is variable to near 80 gauss continuously or to .5 kgauss in the pulsed mode. Base chamber pressures are near 10^{-7} torr and there is a microwave plasma source [Walker, et. al., 1994] located at the far right hand side endcap as shown in the Figure. Plasma densities are variable through this source in a range of $10^3 - 10^9 \text{ cm}^{-3}$ for various gases and electron temperatures range from a few tenths of an eV to 1 eV. The ions are typically near room temperature. The pulsed field which is effectively steady state on the time scale of the experiment has a lower range pulse width of 100 μsec . The chamber has been configured with multiple ports to allow easy access during experimentation. Figure (6) shows the primary experimental arrangement. The essential data acquisition and waveform analysis schemes are based on waveform analysers in portable CAMAC crates, digitizing oscilloscopes, and Macintosh-based LABVIEW II software.

To provide the x-component of the Harris field where,

$$\bar{B}(x,z) = B_{x0} \tanh\left(\frac{z}{\delta}\right) \hat{i} + B_{z0} \hat{k} \quad (14)$$

the grid is pulsed and the field component produced by the pulsed grids adds to the constant z-component produced by the external Helmholtz coils. A typical voltage pulse applied to the inner two grid planes is shown in Figure (16) in an early raw form. The pulse was subsequently flattened by shaping circuits and remained constant over a period of time near 120 μsec . The period within the voltage pulse during

which the data was sampled is indicated by the 50 μ sec window shown on the pulse.

Experiment diagnostics used in the first phase of experimentation consisted primarily of a 3-axis DC Bell gaussmeter, a 3-axis B (dot) loop probe and the forward and backward scattered collector plates seen on either side of the current carrying grid in Figure (6). These instruments are described below.

IV.2 Mechanical Design Considerations

Overview

The experimental operation scenario for this work is shown schematically in the 2D view of Figure (17). Electrons of specified energy are injected in vacuum toward the current carrying mesh. The mesh has dimensions of 1m x 1m and consists of 4 separate planes of tungsten wire carrying equal currents in the same direction. The planes are separated by 1.8 cm. The wires in the meshes are separated by 1.59 mm. The particles are injected into the magnetic field with pitch angle resolution of below 5 degrees. The magnetic field is produced by a combination of the field produced by the mesh and that produced by the external Helmholtz coils of the chamber configuration. The grid structure is referred to as the "quadgrid" model primarily because of the structure of the mesh configuration which contains 4 separate planes as described above. The two large detectors consist of 16 quadrant-sectored current sensor boards each and measure forward and back-scattered electron current.

The experimental scenario requires pulsing for a number of reasons related to the magnitude of currents carried in the wires (near 1 kamp/wire). By digital sampling of the diagnostic instruments we were able to reconstruct both the field and the scattered particles, e.g., once a steady state magnetic field configuration is reached at the end of the current pulse rise time, the electron gun is operated at different accelerating potentials. This is the basic scenario required to experimentally investigate current collection vs electron energy. By pulsing the current, we avoid problems associated with heating and emission at higher current levels and we can also take averages of particle fluxes over many pulsing cycles. In this way it is possible to reconstruct the distribution function from the individual spectra. For definition of the phase space maps the configuration will change with particles being injected in the equatorial plane. When plasma is introduced as a perturbation further problems associated with the self-consistent interaction between plasma and pulsed grids must be considered and the topology restudied in detail. The initial results are vacuum results. This section addresses mechanical design concerns related to the components outlined above.

IV.2.1 Grid Design

The current-carrying grids are shown in multiple schematic views in Figure (7) and (8). Figures (18) and (19) show engineering drawings. The grids were designed using 3/8" - 16 threaded brass rod welded to a T-shaped machined brass support which functions as a current carrying feeder bar. Figure (18) shows dimensions and configuration while Figure (19) shows an end-on view of the brass rods and copper bar. The wire spacing is automatically provided by the threads in the brass rods and this affords a measure of protection as the threaded wire sinks into the grooves and is therefore below the contact level of the rod when placed on a horizontal surface. The wires passing over the the machined brass support are further soldered to the support to insure contact integrity.

As seen from the end-on view to the left in Figure (18), the entire grid structure is designed such that the inner pair of grids slides on insulating supports between the two outer grid planes. With this

arrangement, separate voltages can be applied to inner and outer grids as is in fact the case and covered in Section II above, i.e., the design calls for differing currents in each separate two-grid set. The outer grid structure, which is responsible for the structural support of the entire unit, is supported by 1/2" round fiberglass rods which are bolted to the sides of the structure.

In addition to the grid wires there are magnetic field shaping bars shown in Figure (8) and discussed in Section III. The bars run parallel to the wires at each end as shown and carry varying currents. These bars add primarily a z-component to the field at the position of beam injection and are used to insure that the beam is guided to the grid area for interaction. The magnitude of these currents as discussed above is of the same order as those carried by the grids themselves.

The choice of tungsten wire over copper for the grid windings was governed primarily by the higher tensile strength of tungsten since neither material heats significantly to cause concerns of electron emission in pulse lengths of the order of 50-100 μ sec at current levels near 1 kamp. It was feared, however, that repeated inadvertent contact with the grids could cause stretching and warping of the copper whose Young's Modulus is about a factor of 4 less than tungsten.

Figure (20) is a photograph which shows the grids mounted in the SPSC. Pictured also is the electron gun to the right of the figure. The injection position was later changed to the left of the grids.

IV.2.2 B (dot) Loop Probe

Because of the nature of the pulsed experiment it was necessary to construct a measurement of the magnetic field which would detect the first time derivative of B and integrate it (Hutchinson, 1987). The simplest and most common method of making this measurement at a point in space is to use a loop of wire and exploit the integral form of Faraday's law. To measure 3 components of B we have constructed three orthogonal loops mounted on a common block as shown in Figure (21). Typical current levels of the grids produced magnetic fields are of the order of 10 gauss with rise times between 20 and 50 μ sec. The loops are 1 cm in diameter and consist of three turns of copper wire. A low number of turns is used to limit the inductance for the necessary time response. There is a separate Burr Brown opa 620 differential operational amplifier for each axis as seen in the figure and the emf produced is amplified by a gain 100. Since each axis is independent it is possible to measure simultaneously the rate of change of each component of B. The output of the amplifier is fed to a Tektronix digitizing oscilloscope (TDS 460) and the traces stored and read by Labview* software. To produce the final field strength, DC offsets are removed and the signal integrated with respect to time. Measurement of the steady fields and calibration of the B(dot) loops were performed with a Bell gaussmeter (also 3-axis) Hall probe. As described in Section V below, measurements of the magnetic field during pulsing were made with a resolution of 10 cm across the entire face of the grid structure.

IV.2.3 Current Collector Plates

The photograph of Figure (22) shows the current collectors before installation in the experimental configuration. In this view the 16 sectored collection areas of each plate are easily seen. As mentioned above one primary collection mode in this experiment consisted of ganging together four of the plates horizontally to form 4 rows; current is then sensed to each row independently of which plate collects the current. There was an amplifier attached to each active row of the boards inside the vaccum. The plates

as installed can be seen in perspective with respect to the chamber dimensions in Figure (23). What is shown is the backscattered plate only as the forward plate, being directly behind the grid, is obscured from view. The electron beam accelerator in the lower right hand corner was moved to the left side of the grid during experimentation. All vacuum penetrations to the grid and the collector plate structure were made through a single flange and all penetrations were isolated. We initially encountered noise problems with the bare detector plates and were only able to solve this by covering each plate in a Faraday cage screen and grounding the screen to chamber ground. In fact the wire hanging from the center of the picture is attached to this shield. In addition the plates were biased negatively by 9 volts in order to avoid secondary emission from incident beam electrons. Once these precautions were in place the noise level during pulsing was actually quite low as can be seen in Figures (24) and (25) below; less than perhaps a few mv above background noise levels.

Figures (24) and (25) show back-and forward-scattered current collection as a function of electron beam energy. The data display is taken from a Tektronix TDS 460 digital oscilloscope screen. These figures are displayed to give an overall view of the scattered current collection by the sensor plates. We analyze these Figures in more detail in the following section on Experimental Results.

IV.2.4 Pulsing Forming Network (PFN)

The PFN used to provide the current pulse to the grid is shown in Figure (26). The basic design follows that of Guillemin, [1935]. An example of the applied voltage pulse waveform is shown in Figure (16).

IV.2.5 Electron Beam

The electron beam was provided by the Kimball Physics EMG-14 (50 eV - 10 keV) electron gun and programmable power supply. Current at the injection position varied from 10 to 100 μ A. At these current levels beam spreading at the distances required for injection is negligible. The beam was steerable and approximated to a high degree single particle orbits. It is shown in Figure (27) focussed on a phosphor screen at the approximate beam injection point into the grid area. As mentioned, spreading is quite small over this distance as can be seen in the Figure.

V Experimental Results

V.1 Current collection during pulsing

In Figures (24) and (25) we have plotted the output of the amplifier circuits on each of the backscattered and forward scattered plates using the Tektronix TDS 420 digital display oscilloscope traces. These plots are for the purpose of demonstrating variable levels of current collection as a function of differing electron energy and the shift in enhanced levels of collection with energy and with b_n . Each separate signal represents total current collected by either the forward- or the backward-scattered plate, i.e., there is no sectoring for separate signals as a function of collection position on the plates as is done in a later section. In this following section we compare the energy levels of enhanced collections with those of theoretical predictions at given magnetic field ratios, b_n .

Current collected by both plates is displayed at two different values of B_z in Figures (24) and (25); back-scattered current is the upper trace of the two and forward-scattered is the lower one. In plate 1 of Figure (24) we have indicated the electron beam pulse width; the rise time of the electron beam signal

is on the order of 10's of nanoseconds and throughout the experimental series the beam on-time was adjusted between 20 and 100 μ sec. The beam on-time logic pulse of 100 μ sec is at the top of each plate. In addition the first trace in the upper lefthand corner of Figure (24) is taken with no electron emission (i.e., the current filament of the electron gun is turned off) in order to see the noise background. Major divisions along the ordinate are 20 mv. The conversion between voltage scales on the oscilloscope face and current collected by the sensor plates is a factor of 10^5 , or 1 volt corresponds to 10μ a of collected plate current. It should be noted that pulsing of the grid is taking place during the beam on-time whether the beam is emitted or not; the logic signal is used to pulse both the grids with current and, after a small delay the electron accelerator. The three remaining plates of Figure (24) show various levels of collected currents associated with differing levels of electron beam emission energy.

In Figure (24) the gradual emergence of the backward-scattered signal from noise levels begins to occur as beam energy increases to 400 eV. At 550 eV this level is maximum and then begins to recede as the energy increases further. The forward-scattered signal shows a slight increase during this time but it is clearly the backward-scattered contribution which is dominant.

At lower energy and different field strength it is the forward scattered signal which is dominant as inspection of Figure (25) shows. This signal gradually emerges and recedes in the transition from beam energy of 150 eV to 450 eV.

Each of the figures above is consistent with the general idea of resonance in scattered particle collection as a function of particle energy; in addition, this is also evidence of shifting enhancements in back-and forward-current collection as a function of energy. This will be investigated in more detail below and compared to numerical simulations of particles with different injection distributions.

V.2 Magnetic Field

A complete set of 600 measurements characterizes the entire field region, i.e., the measurement set consists of three separate xy planes on each side of the outer grids separated by $z = \delta$.

Pictured in Figure (28) are the x, y and z components of the pulsed field as measured by the B(dot) loops in the area at $z=2\delta$ from the backscattered grid during pulsing at one particular current level. This figure does not include the constant Helmholtz coil field along z. The units of the figures are multiples of δ , the half width of the magnetic field. The point (0,0) corresponds to the center of the grid, the y-axis is along the direction of current flow in the wire meshes and the x-axis represents distance across the grid perpendicular to the direction of current flow. What is clear from this figure is the relatively constant value of B_x and B_y in the central region of the grid where most of the experiment is performed; on the other hand, the value of B_z varies from a relatively large positive value at the extreme right hand side of the grid ($x=-60$) to a negative value near the left hand side. This variation is largely the undesirable result of the current carrying feeder bars which supply current to the grid wires; there is also some contribution to this result from the current carrying cabling which is attached to the bars although these effects have been largely minimized by favorable geometrical placement and by placing cables carrying current in opposite directions alongside one another. This value of B_z is reversed in sign on the opposite side (forward-scattered) of the grid. The constant value of the Helmholtz coil-produced magnetic field along the z-axis must be added to these values to produce the required modified Harris field configuration of Equation (14).

Although the plots of magnetic field surfaces as shown in Figure (28) are helpful in understanding the magnitudes of the field components they provide little insight into magnetic field direction. Therefore

in an alternate view of the grid produced magnetic field, we show in Figures (29) through (31) vector plots at constant y for better comparison to the modified Harris field form shape. These figures which are the primary interaction region of the beam with the grid show cross sections at $y=68, 78$ and 88 cm from the bottom of the grid. Each of the the figures shows the field produced with no Helmholtz external field, $B_{zH} = 0$, and with $B_{zH} = 4$ gauss. The $z=0$ position corresponds to the center of the grid and $x=0$ corresponds to the left side of the grid in these figures. There is variable linear scaling used on the vector lengths and the grid sizes are symmetric so that the direction of the field vector inferred from the plots is a true indication of the direction in space. The magnetic field along x , B_x , is near 10 gauss for the measurements closest to the grid on the backscattered side but is somewhat reduced from these levels on the forward grid planes. Accompanying these plots is Figure (32) which shows the magnetic field streamlines as derived from graphics software using linear interpolation and 10 cm square resolution. The streamline plots are shown for comparison to the vector routines and were taken only at the $y=78$ cm location. They also do not include as many points as the corresponding vector plot and therefore do not match the structure exactly. It is clear from all of these plots, however, that there is not perfect symmetry in the field produced on either side of the grids; although this would be expected to complicate a comparison of the results to theory the fundamental resonant structure is expected to remain intact.

VI Comparison of Results to theory

VL1 Theoretical resonance dependence on b_n

The positions of resonance peaks as a function of energy are provided by the relation,

$$(N+0.6) \sim \hat{H}^{1/4} \quad (15)$$

where \hat{H} is the normalized Hamiltonian with normalization factor given by ,

$$mb_n^2\Omega_n^2\delta^2 = mb_n^4\Omega_0^2\delta^2 \quad (16)$$

where m is the electron mass, $b_n = (B_z/B_x)$, $\Omega_n = eB_z/mc$, $\Omega_0 = eB_x/mc$ and δ is the half-width of the neutral sheet. For given consecutive peaks N_i , N_{i+1} ,

$$(N_{i+1}+0.6)^4 - (N_i+0.6)^4 = \frac{H_{i+1} - H_i}{mb_n^2\Omega_n^2\delta^2} \quad (17)$$

Consecutive peak separation in energy is therefore predicted to be,

$$mb_n^2\Omega_n^2\delta^2[(N_{i+1}+0.6)^4 - (N_i+0.6)^4] \quad (18)$$

with the peak position in eV given as,

$$H = (mb_n^2\Omega_n^2\delta^2)(N+0.6)^4 \quad (19)$$

The resonant peak separations and positions as a function of energy derived above are based on results of the Harris magnetic field configuration and therefore some differences are expected in terms of the positions of the peaks as a function of energy for the grid field models used in the present work. This is covered in an earlier section and below. Also it should be noted that for large N, the factor of 0.6 can be ignored. However, most of the experimental results presented are for small N number and therefore this form is retained.

VI.2 Simple Theory

In order to evaluate the experimental results it is useful to first consider some simplified physical pictures associated with particle motion in the field. Figure (33) is such a simplified schematic of particle injection into the simulated neutral sheet region (or the plane forming our current grids) at the $z=0$ position. The basic drawing is taken from Chen and Palmadesso, [1986] and shows a transient orbit executing five $z=0$ current sheet crossings, i.e., $N=4$. The original figure has been modified to show the current grids position. The particle scattering collection plates described above are parallel to the $z=0$ plane and spaced a few δ on either side of the grids. The plates themselves along with the magnetic field lines are omitted from this drawing for clarity but recall that the magnetic field has only an x, z component in the modified Harris form.

Turnaround points in Z

If B_z is taken near zero (or if b_n is small) particle motion within the current sheet can be considered as nearly motion in a pure neutral sheet [Sonnerup, 1971] so that the problem can be viewed at fixed x as in Figure (34) and motion is considered only in the yz plane. There is a pure oscillation in this plane with the position of the turn-around point in z_t only a function of the injection angle at the edge of the sheet and the Larmor radius in the field, B_x . This is equivalent to considering only the component of the injection velocity which is perpendicular to B_x at injection, i.e., since we assume small b_n [Kaufmann and Lu, 1993; Chen and Palmadesso, 1986]. This case, which is simpler to analyze than the three dimensional case, can provide insight into particle motion and turn-around conditions in the current sheet field.

It is easy to show under the assumptions above that the positions of the turning points for the planar single particle motion described are given by [Chen and Palmadesso, 1986; Sonnerup, 1971],

$$z_t = \pm \sqrt{2\rho_0 \delta (1 - \cos\alpha)} \quad (20)$$

where $\rho_0 = V_\perp / \Omega_0$ is the particle Larmor radius at the $z=0$ plane, Ω_0 is the cyclotron frequency in the field B_x and α is the angle between V_\perp and the y -axis. Since, in order to turn around, the particle must be within one Larmor radius of the neutral sheet edge where B_x is maximum this implies that $z_t \max \approx \delta$ or $\rho_0 = \delta/2$ or from Equation (20),

$$\sqrt{2\rho_0 \delta} \leq \delta \quad (21)$$

Equation (20) may also be re-expressed as,

$$z_t = \pm (2mE_\perp)^{1/4} \sqrt{\frac{2\delta(1-\cos\alpha)}{eB_x}} \quad (22)$$

or,

$$z_i = \pm \sqrt{\frac{2\delta p_{\perp}(1-\cos\alpha)}{eB_x}} = \pm \sqrt{\frac{2\delta(p_{\perp}-p_y)}{eB_x}} \quad (23)$$

where p_{\perp} is the perpendicular component of particle momentum. From Equations (22) and (23) it is apparent that the turnaround positions in z are a function of both total energy and the angle α . In the general case there is a contribution both perpendicular and parallel to B due to the x -component of the injection velocity.

Dependence of resonant peaks on perpendicular energy

As seen from the above the particle turning points in z are a function of particle momentum along z , the half width of the current sheet (δ) and the magnetic field along x . It might be noted also that the smaller the ratio $b_n (=B_{z0}/B_{x0})$ the more closely the approximation here resembles the actual injection scenario. However, the resonance condition does not have an explicit dependence on this ratio as is seen in Equation (21). It should be noted at this point that the definition of the Larmor radius, $\rho_0 = p_{\perp}/eB$, as traced through Equations (21) through (23) above, allows relatively higher injection energies depending on the single particle injection angle with respect to the magnetic field, i.e., the criterion of Equation (21) can be satisfied for higher total energies than at first would appear. This can be seen from the following simple argument based on the resonance condition of Equation (15). We note that the normalization factor of Equation (16) can be expressed as,

$$mb_n^4\Omega_0^2\delta^2 = mb_n^4\left(\frac{v_{\perp}}{\rho_0}\right)^2\delta^2 \quad (24)$$

where v_{\perp} is the component of injection velocity perpendicular to B_x . Expressing this in terms of a perpendicular energy we can re-express \hat{H} as,

$$\hat{H} = \frac{H}{2E_{\perp}b_n^4\left(\frac{\delta}{\rho_0}\right)^2} \quad (25)$$

Using the turn-around condition expressed in Equation (21) to define the minimum value of the normalization constant, we have,

$$N_{\max} = \hat{H}_{\max}^{-\frac{1}{4}} = \left(\frac{H}{8E_{\perp}b_n^4}\right)^{\frac{1}{4}} \quad (26)$$

or the maximum number of resonances observable depends upon the energy component perpendicular to x and is therefore also a function of the injection pitch angle.

There is, however, a complicated dependence of the injection pitch angle with respect to the initial field at the injection position and the field at the turnaround position. For example, in the limit that $B_x \ll B_z$ essentially all of the particle energy for nearly field aligned injection would be injected perpendicular to the small B_x value; as injection energies increase therefore, one would expect to encounter the limit of Equation (21) fairly quickly. However, in the opposite limit when $B_x \gg B_z$ (small

b_n) nearly field aligned injection would be essentially along B_x with a small component perpendicular to x . In this case and generally for relatively small values of b_n one can inject high particle energies and observe resonances predicted due to the small component of E_\perp and thus the satisfaction of the boundary condition of Equation (21). This is the case for most of the experimental work performed and described here. Indeed, it is the intermediate case which we observe to produce the resonant structures for our injection scenarios which include a 10-15 degree cone about the field direction..

VI.3 Results from the numerical work

Our primary injection pitch angle was near field aligned (or 180 degrees from field alignment) for most of the experimental work presented here. The numerical simulations described above were performed for 3 different injection distributions at fixed values of b_n . The results presented in this section are based on injection of a ring distribution into either the modified Harris field or the quad-grid field. The cone angle of this injection is in all cases less than 10 degrees from field alignment (or anti-parallel to field alignment)

Figures (35) and (36) show the coherence factor, C_r , defined earlier, versus the normalized Hamiltonian values of Chen and Palmadesso. Each of the plots is performed for the ring distribution at injection and for different values of b_n . Each figure is for two values of b_n and includes both the modified Harris distribution in addition to the experimental configuration as simulated numerically and described earlier. Figures (35a,c) and (36a,c) are for the Harris case and Figures (35b,d) and (36b,d) are for the quad-grid model. A conclusion which arises from these plots is that there appear resonant structures extending to higher and higher values of $\hat{H}^{1/4}$ for decreasing values of the ratio b_n in the near field aligned injections in the numerical program, i.e., there are more peaks extending to higher values of the normalized energy as one traces the figures from Figure (35) through Figure (36) in which b_n changes from .3 to .6. This is consistent with the arguments above which, through Equation (21), show that the maximum number of neutral plane crossings is inversely proportional to both the ratio b_n and the perpendicular component of injection energy. When the injection angle is varied much above the approximately 10 degree cone angle about field alignment, the resonant structures seen in these figures begin to disappear both in the case of the Harris field and for the case of the experimental scenario. This behaviour is seen for the Harris field distributions in Figure (37) in which injection pitch angles of 20,30 and 50 degrees are shown in increasing order from bottom to top of the page. Energy ranges in these figures are not as broad as in earlier Figures 35 and 36 but they may nevertheless be compared for peak structure to Figure (35a). (Note that the abscissa scale in the plots of Figure (37) are in units of $b_n \hat{H}^{1/4}$ so that to compare the peak positions with Figures (35) and (36) one divides the abscissa values of Figure (37) by b_n).

It should be noted that, with the normalization scheme of Chen and Palmadesso, [1986] as described in Equation (15) a value of B_x and b_n must be specified in order to calculate the actual energy in eV as can be seen through Equation (19). As an example of this calculation, an $N=2$ (i.e., $\hat{H}^{1/4}=.6$) resonance at $b_n=.2$ and $\delta=10$ cm would occur at an energy of about 128 eV for $B_x=10$ gauss, at about 650 eV for $b_n=.3$ and when b_n is increased to .4 this energy increases to near 2 keV. Our primary energy operation range in the experiment varied from about 250 eV to several keV as is seen in the results of the next section.

VI.4 Experimental Results

The experimental results were obtained at three different grid current levels which produced three different levels of B_x . In each case the external Helmholtz field B_z was changed to produce a b_n variation.

VI4.1 Resonances

A dramatic example of the type of resonant behaviour observed during experimental cycles is provided by Figures (38) and (39) which show forward scattered current collection for the $B_x = 12$ gauss field in Figure (38) and the highly structured coherence factors for the same data set in Figure (39). Note that the backscattered contribution is the complement of the forward scattered data. Both figures are plotted for two different values of the external Helmholtz coil field B_H increasing from the bottom of the page (Recall that B_H is not the same as the total B_z as covered in Section V.2 above and so one cannot generate b_n simply by dividing this value by B_x). The shift of the primary forward scattered resonance peaks in Figure (38) from $\hat{H}_D^{1/4} \sim 0.87$ (bottom panel) to $\hat{H}_D^{1/4} \sim 0.97$ (top panel) is evident as B_H increases; also the backscattered peak seen in the C_r plots as the second enhancement near about $\hat{H}_D^{1/4} \sim 0.93$ in the lower plot of Figure (39) increases in a similar manner to the rather broad peak extending from $\hat{H}_D^{1/4} \sim 1.06$ to $\hat{H}_D^{1/4} \sim 1.15$ in the upper panel. This feature of shifting peak position as the primary field varies is consistent throughout the experimental work. These two Figures may be compared to Figures (11) through (13) of the numerical simulation for the "quad grid" model described earlier. Figure (40) is a plot of C_r vs $\hat{H}^{1/4}$ in order to allow one to compare to the numerical plots presented earlier and the primary Equation (15). In this case and for earlier definitions, $N+1$ refers to the number of neutral sheet crossings so, for example, for $N=1$ and electron injection on the backscattered side (by definition), one expects a peak in the backscattered current relative to the forward scattered side; $N=2$ would imply resonance in forward scattered collection, etc; note that $N=0$ would imply a single crossing.

A similar behaviour is seen in Figures (41) and (42) which are a plot of the normalized forward-scattered current for two different values of the external field B_z for the case in which B_x is 5.6 gauss. In these plots the peaks have been expanded to show more clearly the energy shift as the external Helmholtz coil field is varied.

It should be pointed out that the numerical values of $\hat{H}^{1/4}$ seen in Figure (40) cannot be used as the primary basis of comparisons to theory. Resonances on these scales are separated by $\Delta\hat{H}^{1/4}$ values more on the order of 0.2 than 1 as predicted by the theory. The explicit dependence of N on the power of \hat{H} is closely associated with the perfectly realizable Harris field and is not expected to characterize scattering centers which in general show chaotic scattering dependence on initial conditions but do not have exactly this field form [Chen, 1993]. Also the normalized energy as seen in Equation (15) is a function not only of the field but also of the parameters b_n and δ both of which are to some extent variable in the experiment; b_n varies with respect to position as discussed earlier and δ is estimated to include finite effects of near-wire distortions in the field. The values of N are highly sensitive to the choices of these two parameters in the normalization; it is the resonance structuring itself and its dependence on the initial conditions of energy and magnetic field that determine chaotic scattering from the scattering center.

For comparison to predictions of the Harris model and the simulations we show in Figure (43) the explicit energy dependence of the first two scattering resonances on the ratio b_n . Figures 43(a) and 43(b) show numerical simulations and Figure 43(b) shows the analytic energy dependence of the Harris model. We note that the dependence of the energy separation of the two peaks on b_n is qualitatively similar to what is observed in the laboratory case explored above in Figure (38).

VL4.2 Collected Current as a Function of y

As the energy of the injected particle is increased the particles leave the current sheet at higher and higher values of the y-coordinate. This is due to the fact that increasing energy implies increasing numbers of neutral sheet crossings and therefore detected particles travel farther in the y-direction. This behaviour which was demonstrated in Table I for the numerical simulation in the quad grid model case can also be seen in Figure (44) in which we plot three different injection energies for the case of the Harris field simulation for $B_x = 12$ gauss at low pitch angle. This figure shows the final y-position (whether collected by the back-scattered or the forward scattered plate) increasing with energy, E, and with N, where N+1 is the number of z-plane crossings. These two quantities increase going from plate (a) through (c) of the Figure. The trajectories are stopped at the positions of the collector plates and with these dimensions one can see that even for the 5 keV case of part (c) the particle emerges within the boundaries of the grid region. Each of these injections corresponds to a nearly field aligned injection and the position of the electron gun is as it was in the experiment. Figure (45) shows the number of scattered particles at different y-levels of collection as a function of energy for the numerical simulation of the actual field configuration produced by the grid and shaping bar assembly. Again the current collection levels increase with increasing y. Plotted in Figure (46) is the centroid of experimental current collection as a function of beam energy. As mentioned earlier both forward and backward scattered collection plates are partitioned into 16 separate plates; for this study the plates were ganged into groups of four along the x direction producing 4 separate horizontal rows. Total collected current is then monitored to each row as a function of energy. For the case chosen Figure (46) shows the current collected by the first two (lowest) forward scattered collection plates. The straight lines drawn represent the best fit to indicate average behaviour. The behaviour of the centroid of current is a result of decreasing collected current as a percentage of total on the first plate while that collected on the upper plate shows a corresponding increase.

One might reasonably ask whether the observed increase in y-position is simply the result of an increased Larmor radius due to the energy increase. Since this increase should go as the square root of energy one would expect current collection to follow the 1/2 power law given by this equation and to observe a broadening of the average pattern of collected current but no shift in the center position. This is not consistent with the observations of Figure (46) which plot the centroid of collected current on the plate. Without the resonances as described above it is difficult to explain the shifting energy peak patterns observed.

Figure (47) shows a plot of the correlation factor C_r described above vs $\hat{H}^{1/4}$ except that instead of plotting the back and forward scattered peaks as positive values, forward scattered peaks are plotted as negative values. In this presentation it is easier to isolate forward from back scattered contributions without suppressing either. The relatively high value of the external B_z field produces a small b_n component on the forward grid side and a much larger one on the backscattered side. This behaviour is seen in Figures (29) through (31) which are plotted for a different value of current in the grids.

VII Scaling Considerations and Future Work

In making comparisons to the insitu measurements a key issue is how and to what extent the expected laboratory results may be related to the actual space environment. Although as mentioned we did not attempt to build a model system, the basic physical processes rely on scale sizes. The most

important quantities are the spatial scale lengths and their relationship to one another. The relevant physical parameters are: the particle gyroradius ρ , the radius of curvature of the field lines in the current sheet R_c , the current sheet thickness δ , the field component ratio b_n , gyrofrequency Ω_n , and the particle energy. Scaled values of typical neutral sheet parameters are listed in Table II using length scaling to the experimental basis [e.g., Faelthammar, 1974]. The particle dynamics is stochastic rather than adiabatic in the current sheet because the gyroradii of the particles can be comparable to the radius of curvature of the field lines in the current sheet. In the magnetotail, a large fraction of the ions are in the nonadiabatic regime under quiet-time conditions, a fact which has been known for some time [Speiser, 1965]. Some electrons are also in the nonadiabatic (and nonintegrable) regime [West et al., 1978a,b; Lyons, 1984]. For the modified Harris model, the radius of curvature at $z = 0$ is $R_c = b_n \delta$. If $\rho_n = R_c$, then the motion is highly nonadiabatic. Note that R_c/ρ_n is a dimensionless statement. The resonance scaling law above is expressed in terms of the dimensionless normalized Hamiltonian. The relevant physical parameters are b_n which is the dimensionless ratio B_n/B_0 , $\Omega_n = v/\rho_n$ and δ . Thus the resonance condition can be directly scaled to the laboratory distribution functions. For example, the separation between two resonances N_1 and N_2 is, as treated in Section VI.1, $\Delta(H^{1/4}) = (mb_n^2 \Omega_n^2 \delta^2)^{1/4} (N_2 - N_1)$ [Burkhart and Chen, 1990]. It was also shown that the resonance peaks are strong for, $H \leq H_1 = (1/2)b_n^{-2}$ and that the distribution resonance peaks should terminate for the condition $H \geq H_2 = (1/2)b_n^{-4}$. These properties are all expressed in terms of dimensionless parameters. Thus they are easily amenable to laboratory simulations.

In order to accomplish Objective (iii) of Section IIa. we point out that having once established the scaling law, Chen et al.,[1990] have argued that the characteristic thickness of the current sheet could be measured by the particle distribution function outside the current sheet. For a thermal distribution of current carriers, they showed that,

$$\delta = \alpha^2(8/\pi) \Gamma^2(7/4) \rho_t$$

where α is a factor of order unity to be determined, Γ is the gamma function and ρ_t is the Larmor radius of a thermal particle evaluated outside the current sheet ($z > \delta$). This relationship is important because it relates the observed distribution function features obeying the scaling law to the thickness of the current sheet. The parameter α will be calculated theoretically separately. Future laboratory experiment simulations can test this theoretical prediction under various controlled conditions. The result can be scaled straight forwardly to the magnetotail environment. Conversely, theoretical results can be scaled to the laboratory parameters to be tested. In this regard, we note that we have a computer code to construct surface of section plots for a given magnetic field configuration (not limited to the fields that may be generated in the space chamber). We expect to control surface of section plots for the experimental magnetic field geometry. In fact, we will run numerical studies of orbits in the laboratory fields.

We note that in the experimental setup, the magnetic field as seen in Figures (28) through (32) is not perfectly smooth and is x -dependent. Holland and Chen [1991], however, have shown that fluctuations in the magnetic and electric fields under quiet-time magnetotail conditions do not significantly affect the scaling behavior and that energy gain/loss (ΔH) for collisions comparable to the difference between two neighboring resonances must be present to significantly degrade the resonance effect. Relative to the x -dependence, Burkhart and Chen [1991] have shown that if $\rho_n < L_x$, where L_x is the gradient scale length in the x -direction, then the scaling law is not affected. This condition again is expected to be well satisfied.

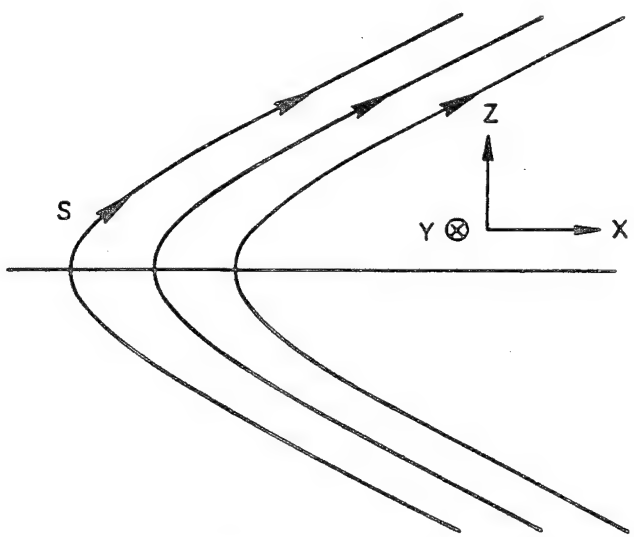
ACKNOWLEDGEMENTS:

This work was funded by the Office of Naval Research. Also, we wish to acknowledge discussions with a number of people regarding this work. Useful suggestions were provided by Prof. D. Papadopolous, University of Maryland, Prof. W. Gekelman, UCLA and Prof. R. Kaufmann of the University of New Hampshire.

VIII REFERENCES

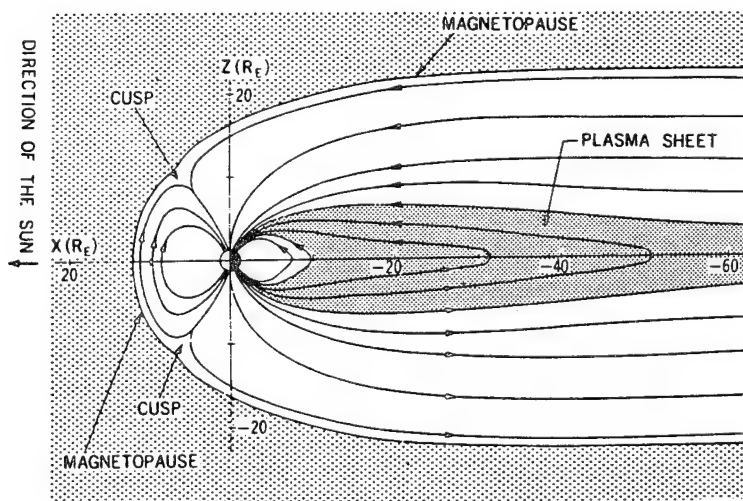
- Alekseyev, I.I., and A.P. Kropotkin, Geomagn. Aeron., Engl. Transl., 10, 615, 1970.
- Alfven, H., L. Danielsson, C.-G. Faelthammar and L. Lindberg, Proc. Plasma Space Sci. Symp., the Catholic University of America, Washington, DC, 1963.
- Alfven, H., NATO advanced study institute held in Bad Homburg, Germany, p.33, Plenum Press, New York, July 1964.
- Alport, M.J., S.L. Cartier, and R.L. Merlin, J. Geophys. Res., 91, 1599, 1986.
- Ashore-Abdalla, M., J. Berchem, J. Buechner, and L.M. Zelenyi, Geophys. Res. Lett., 17, 2317, 1990.
- Block, L.P., Planet. Sp. Sci., 15, 1479, 1967.
- Block, L.P., Tellus, 7, 65, 1955
- Block, L.P., Tellus, 8, 234, 1956.
- Buechner, J. and L.M. Zelenyi, Phys. Lett. A, 18, 395, 1986.
- Buechner, J. and L.M. Zelenyi, J. Geophys. Res., 94, 11821, 1989.
- Burkhart, G.R. and J. Chen, J. Geophys. Res., 96, 14033, 1991.
- Chen, J. and P.J. Palmadesso, J. Geophys. Res., 91, 1499, 1986.
- Chen, J., G.R. Burkhart, and C.Y. Huang, Geophys. Res. Lett., 17, 2237, 1990a.
- Chen, J., H.G. Mitchell, and P.J. Palmadesso, J. Geophys. Res., 95, 15141, 1990b
- Chen, J., Phys. Fluids B, 5, 2663, 1993.
- Cowley, S.H.W., Cosmic Electrodyn., 2, 90, 1971.
- Doxas,I., W. Horton, K. Sandusky, T. Tajima, and R. Steinolfson, J. Geophys. Res., 95, 12033, 1990.
- Eastwood, J.W., Planet. Sp. Sci., 20, 1555, 1972.
- Faelthammar, C.-G., Sp. Sci. Rev., 15, 803, 1974.
- Fahleson, U., Planet. Sp. Sci., 15, 1489, 1967.
- Gekelman, W., 86, 659, 1981.
- Hairapetian, G. and R.L. Stenzel, Phys. Rev. Lett., 65, 175, 1990.
- Holland, D.L. and J. Chen, Geophys. Res. Lett., 18, 1579, 1991.
- Horton, W. And T. Tajima, Geophys. Res. Lett., 17, 123(1990)
- Huba, J.D., J. Chen, and R.R. Anderson, J. Geophys. Res. (1991).
- Hutchinson, I.H., Principles of Plasma Diagnostics, Cambridge Univ. Press, 1987
- Kaufmann, R.L., D.J. Larson, P. Beidel and C. Lu, J. Geophys. Res., 98, 9307, 1993
- Kaufmann, R.L., D.J. Larson, P. Beidel and C. Lu, J. Geophys. Res., 98, 9321, 1993
- Kaufmann, R.L. and C. Lu, J. Geophys. Res., 98, 15447, 1993
- Kawashima, N. and S. Mori, Phys. Fl., 8, 378, 1965.
- Koepke, M. And W.A. Amatucci, Phys. Rev. Lett., 72, 3355, 1994
- Lyons, L.R., J. Geophys. Res., 89, 5479, 1984.
- Lyons, L.R. and T.W. Speiser, J. Geophys. Res., 87, 2276, 1982.
- Martin, R.F., J. Geophys. Res., 91, 11985, 1986.

- Pellat, R., Phys. Fluids, 22, 381, 1979.
- Schindler, K., Rev. Geophys., 7, 51, 1969.
- Sonnerup, B.U.O, J. Geophys. Res., 76, 8211, 1971.
- Speiser, T.W., J. Geophys. Res., 70, 4219, 1965.
- Speiser, T.W., J. Geophys. Res., 72, 3919, 1967.
- Speiser, T.W., and L.R. Lyons, J. Geophys. Res., 89, 147, 1984.
- Stenzel, R.L. and W. Gekelman, J. Geophys. Res., 86, 649, 1981.
- Stern, D., and P. Palmadesso, J. Geophys. Res., 80, 4244, 1975.
- Swift, D., J. Geophys. Res., 82, 1288, 1977.
- Wagner, J.S., J.R. Kan, and S.I. Akasofu, J. Geophys. Res., 84, 891, 1979.
- Walker, D.N., J. Geophys. Res., 91, 3305, 1986.
- Walker, D.N., P.K. Chaturvedi, M. Singh, P. Rodriguez and C.L. Siefring, J. Geophys. Res., 96, 3589, 1991.
- West, H.I., R.M. Buck, and M.G. Kivelson, J. Geophys. Res., 83, 3805, 1978a.
- West, H.I., R.M. Buck, and M.G. Kivelson, J. Geophys. Res., 83, 3819, 1978b.



Schematic drawing of the Harris-type magnetic field (equation (1)) and the coordinate system. The line segment s measures the distance from $Z = 0$ along the magnetic field lines.

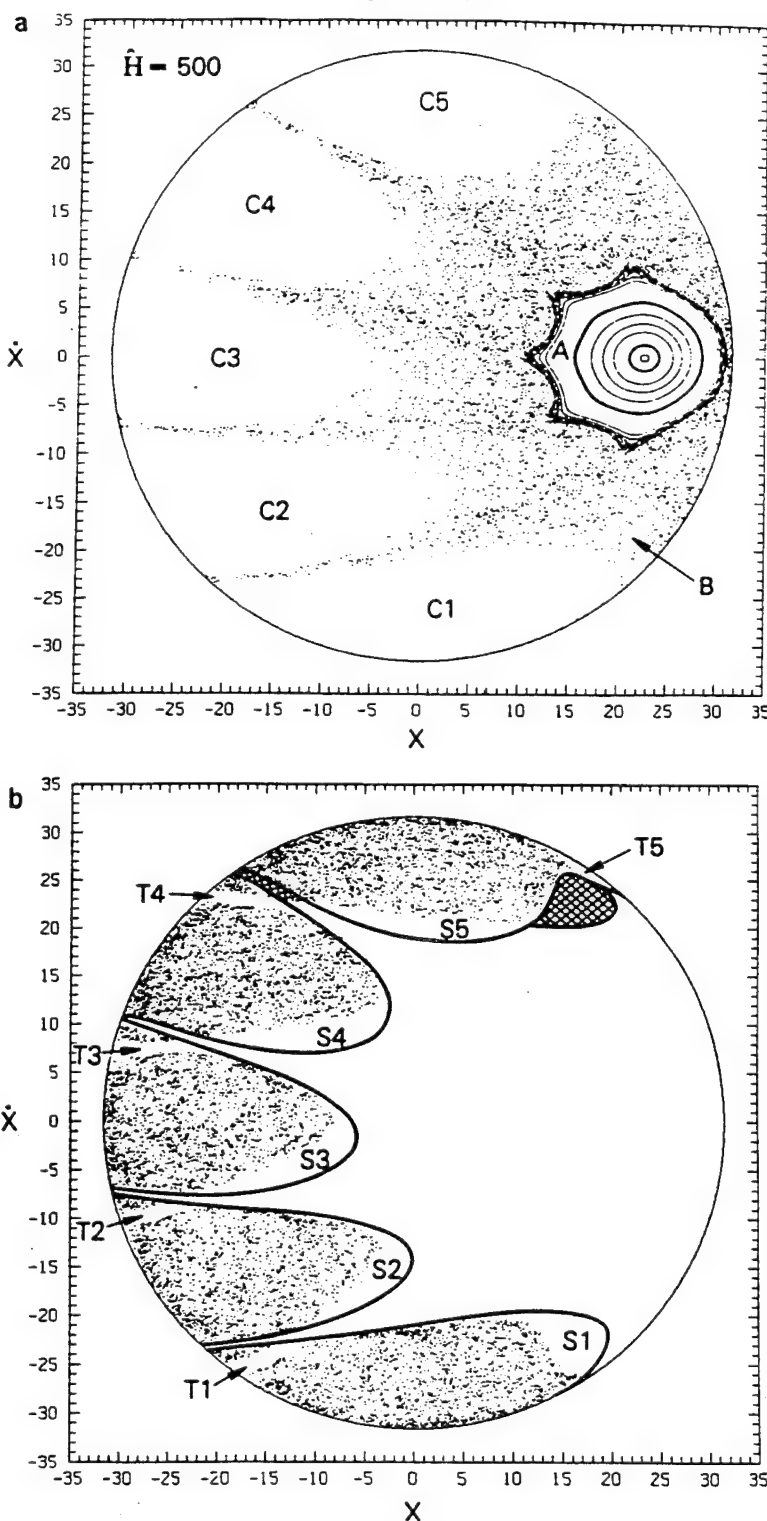
Figure (1)



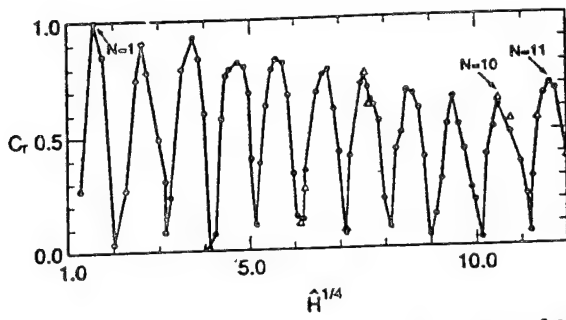
Schematic illustration of the noon-midnight section of the magnetosphere.

Figure (2)

Figure (3)

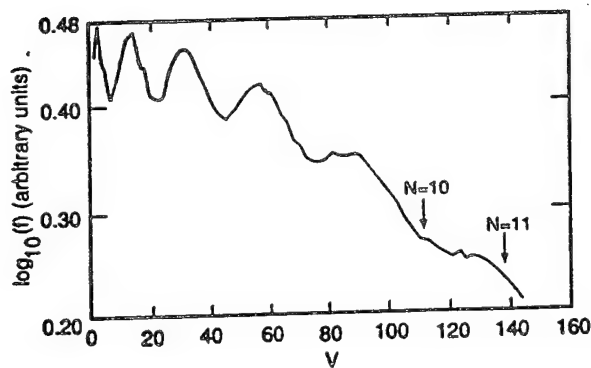


Surface of section plots for the Harris-type field with $b_r = 0.1$ and $\hat{H} = 500$. (a)-Representative integrable orbits in region A and stochastic orbits in region B; 60,000 points. (b) Transient orbits, showing the substructures in regions C1-C5; 42,000 points.



Plot of the coherence factor C_r versus $\hat{H}^{1/4}$.
 $b_n = 0.05$. The number of orbits for each energy is 355
(solid circle) or 598 (triangle). Straight lines are drawn
between points. Peaks for $N = 1, 10$ and 11 are shown.

Figure (4)



A model steady-state distribution function $f(v)$ at
 $z = +3\delta$ with $b_n = 0.05$. $f_1 > f_2$ is assumed.

Figure (5)

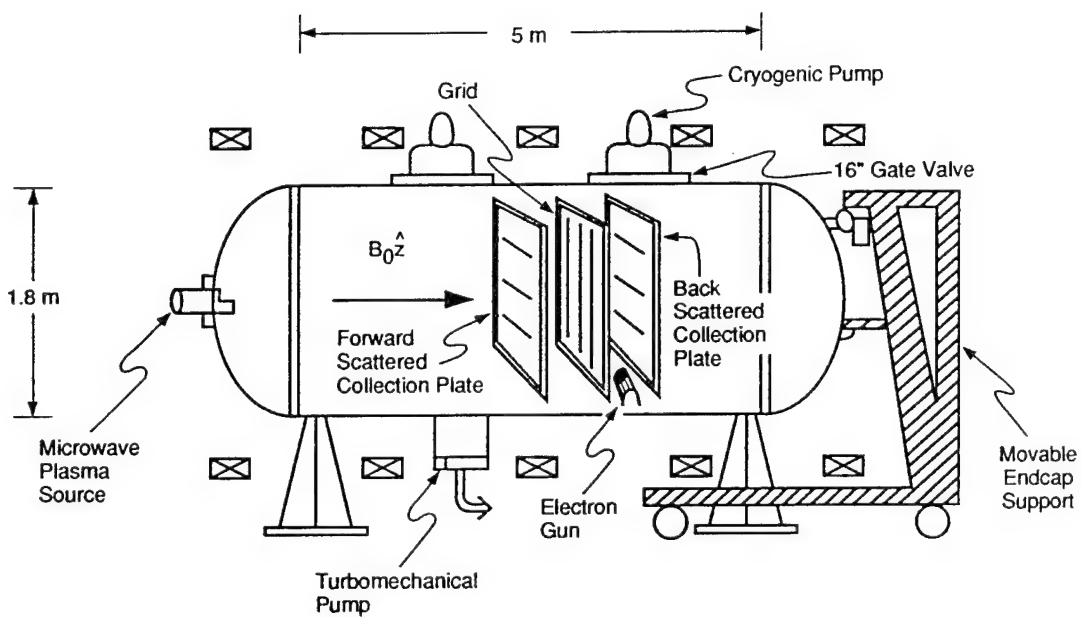
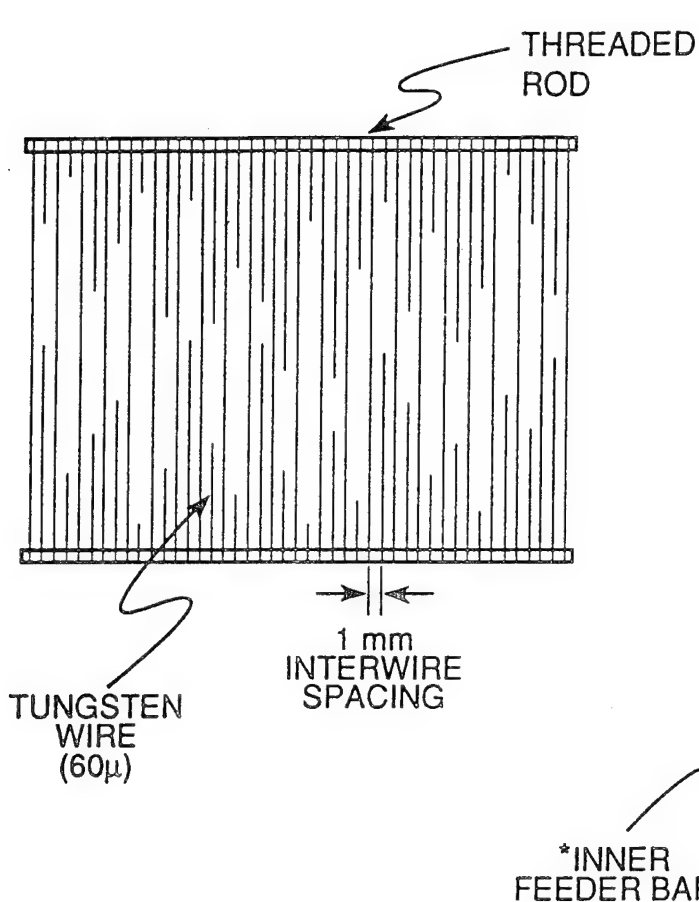
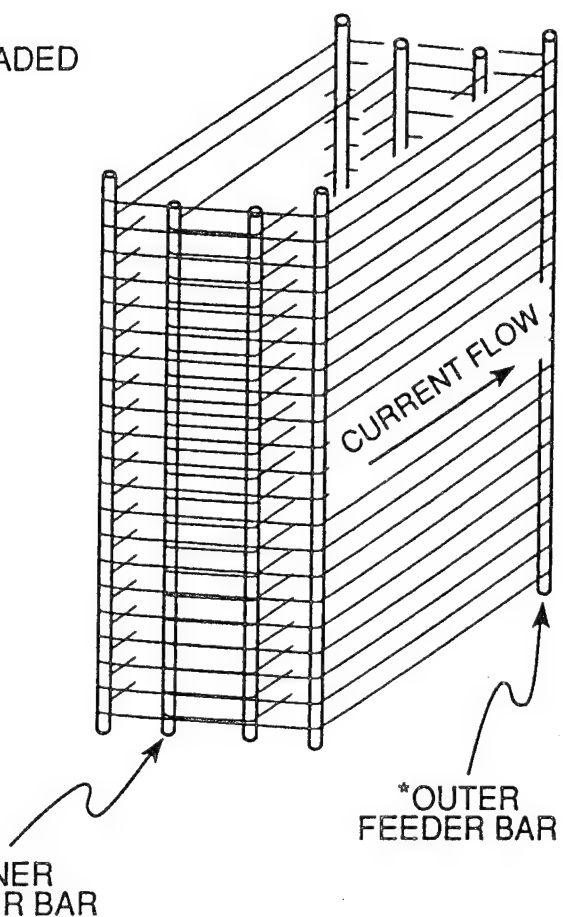


Figure (6)

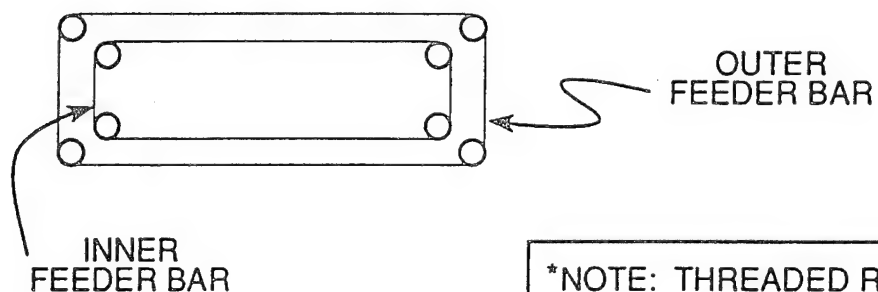
SINGLE GRID STRUCTURE
(FRONT VIEW)



FOUR GRID STRUCTURE
(ANGLED VIEW)

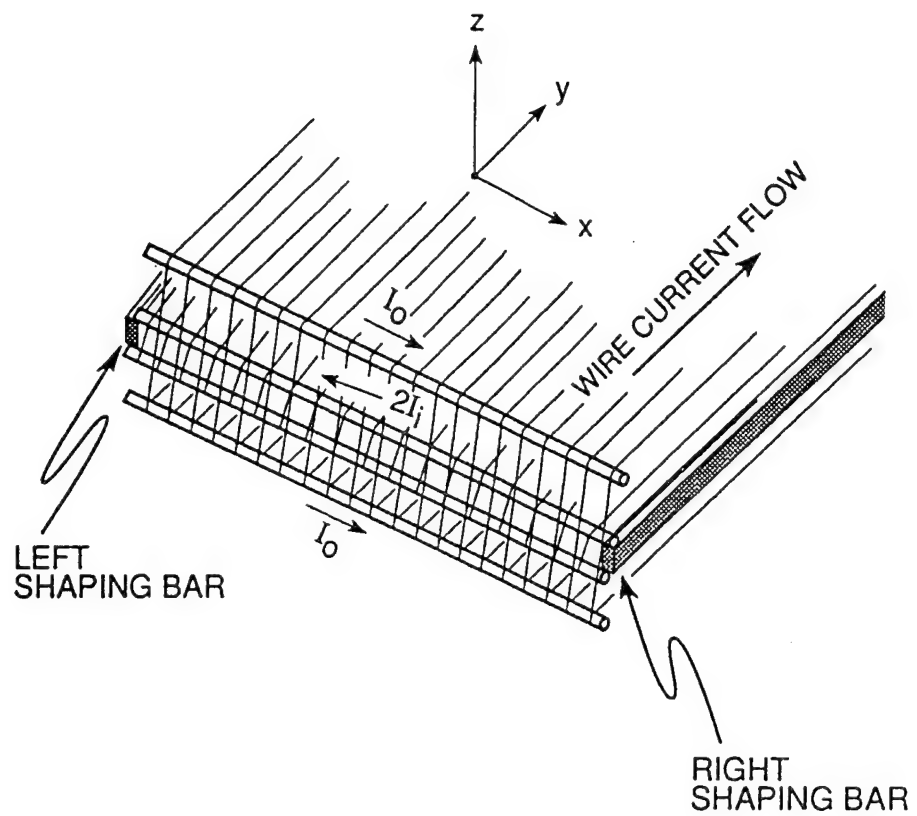


TOP VIEW



*NOTE: THREADED RODS ARE ATTACHED
TO EITHER SIDE OF CONDUCTING
FEEDER BAR (NOT SHOWN).

Figure (7)



Grid showing shaping bars,
feeder bar current directions, and
orientation. z is along chamber z axis.
Feeder bars are not shown.

Figure (8)

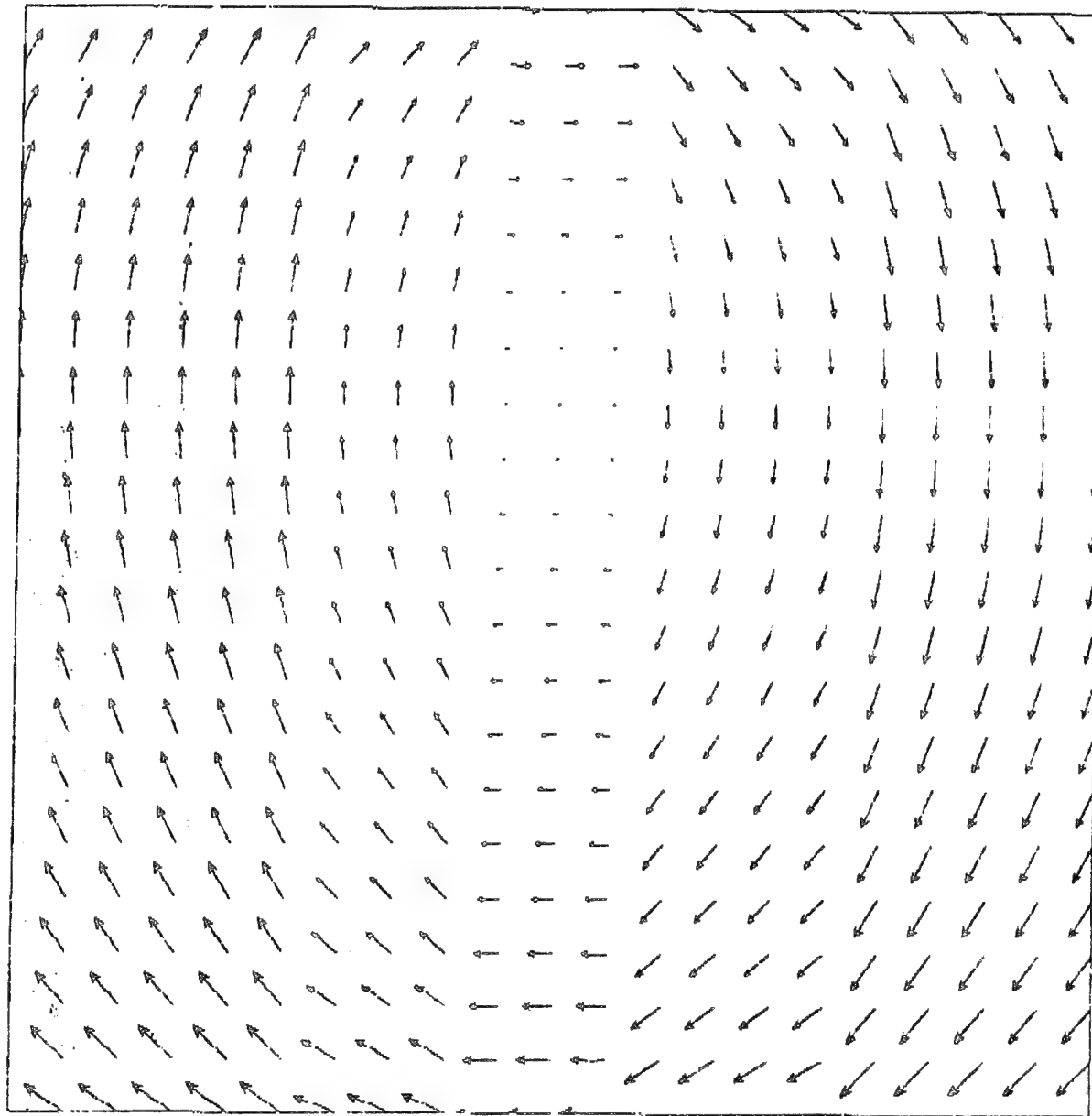


Figure (9)

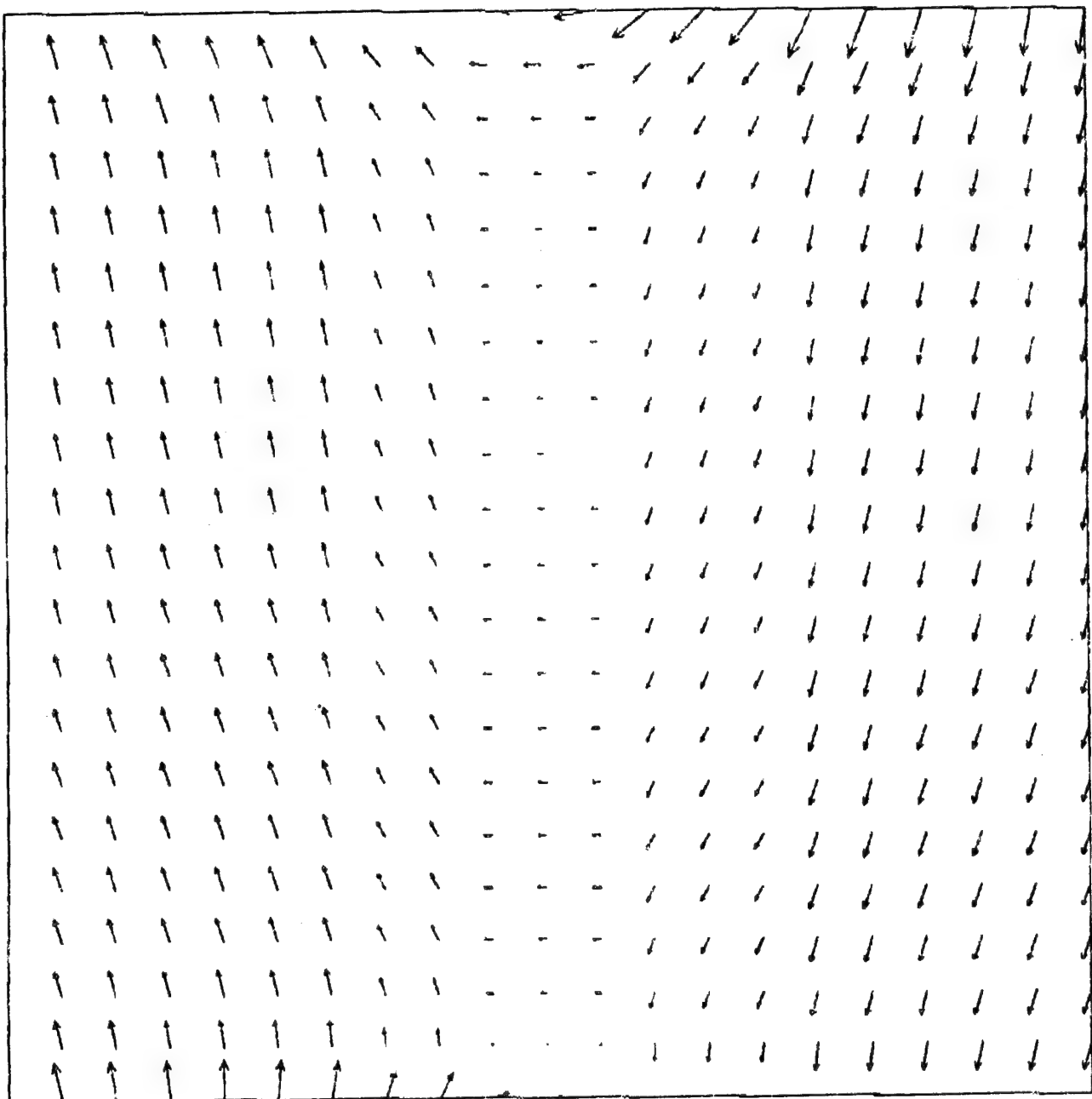
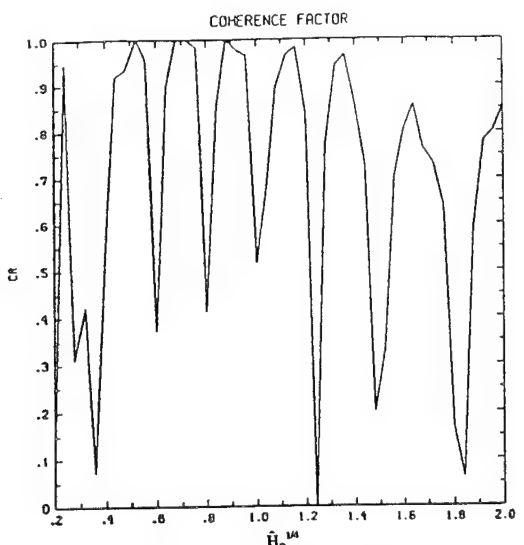
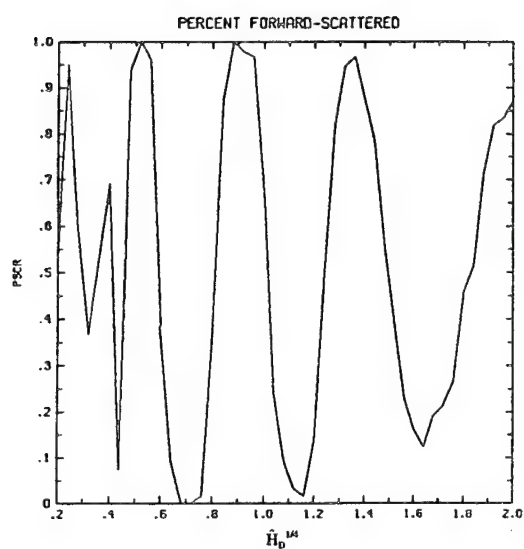


Figure (10)

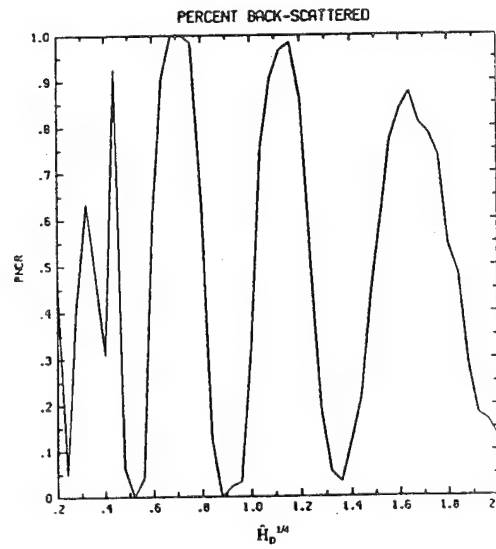


Plot of Coherence factor CR versus $\hat{H}_D^{1/4}$

Figure (11)



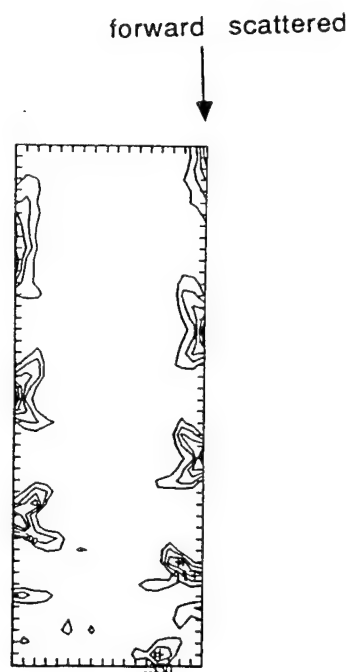
Percentage of particles forward scattered versus $\hat{H}_D^{1/4}$



Percentage of particles backward scattered versus $\hat{H}_D^{1/4}$

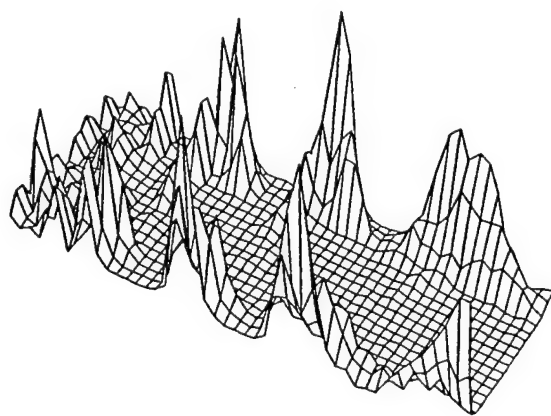
Figure (12)

Figure (13)



Electron scattering amplitudes versus
pitch angle

Figure (14)



Electron scattering amplitudes versus
pitch angle - 3 dimensional view

Figure (15)

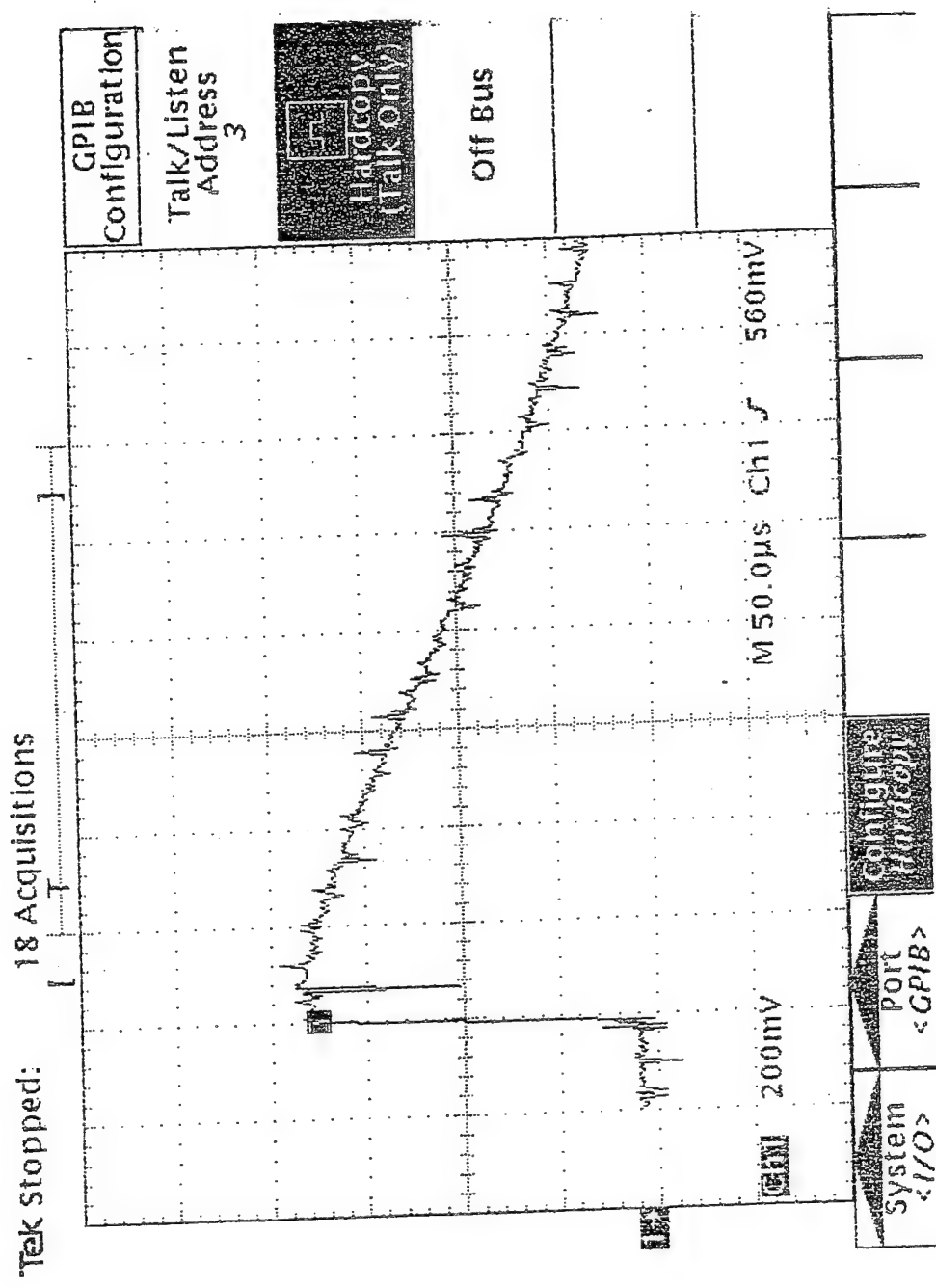


Figure (16)

SPSC SCHEMATIC WITH HARRIS TYPE FIELD

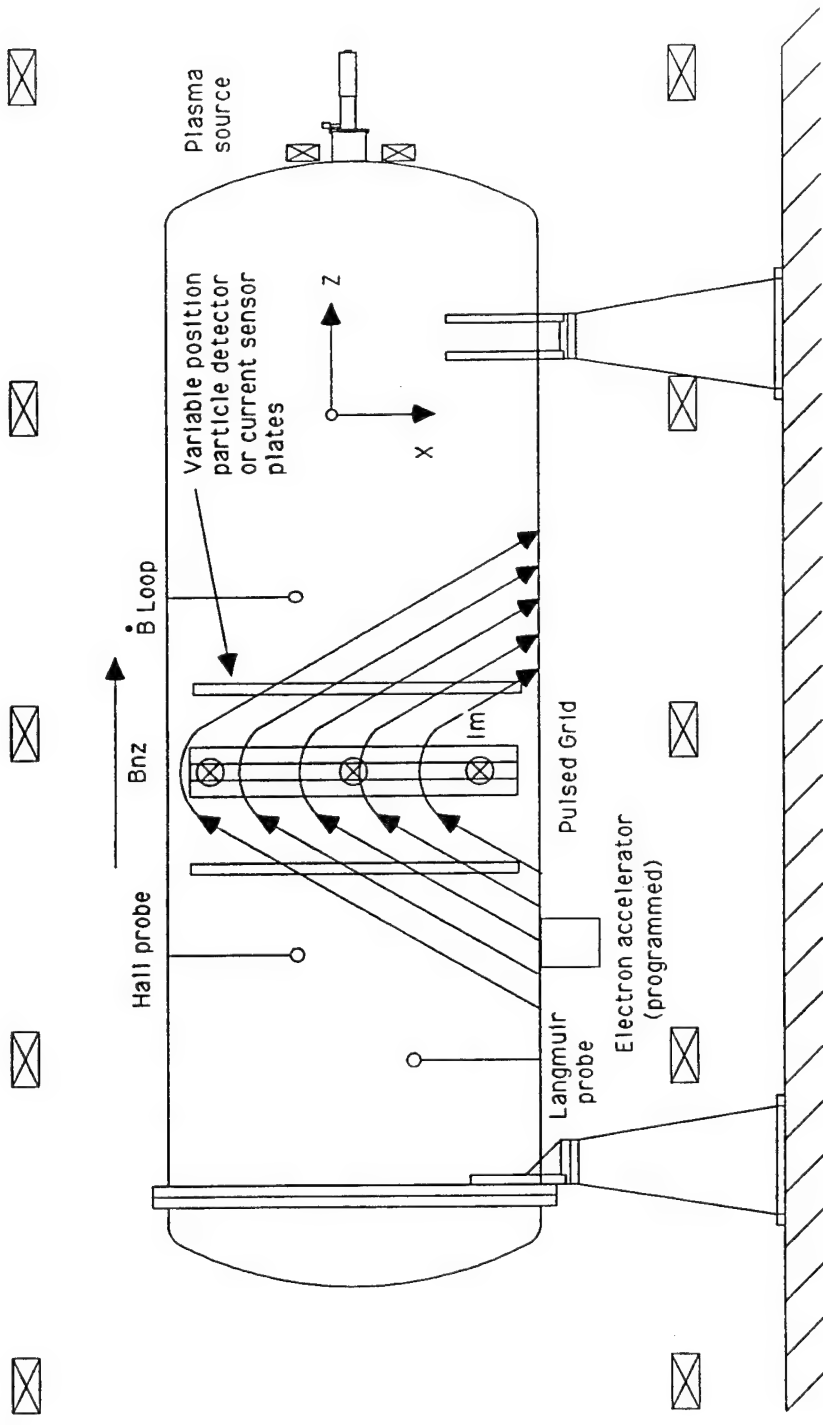


Figure (17)

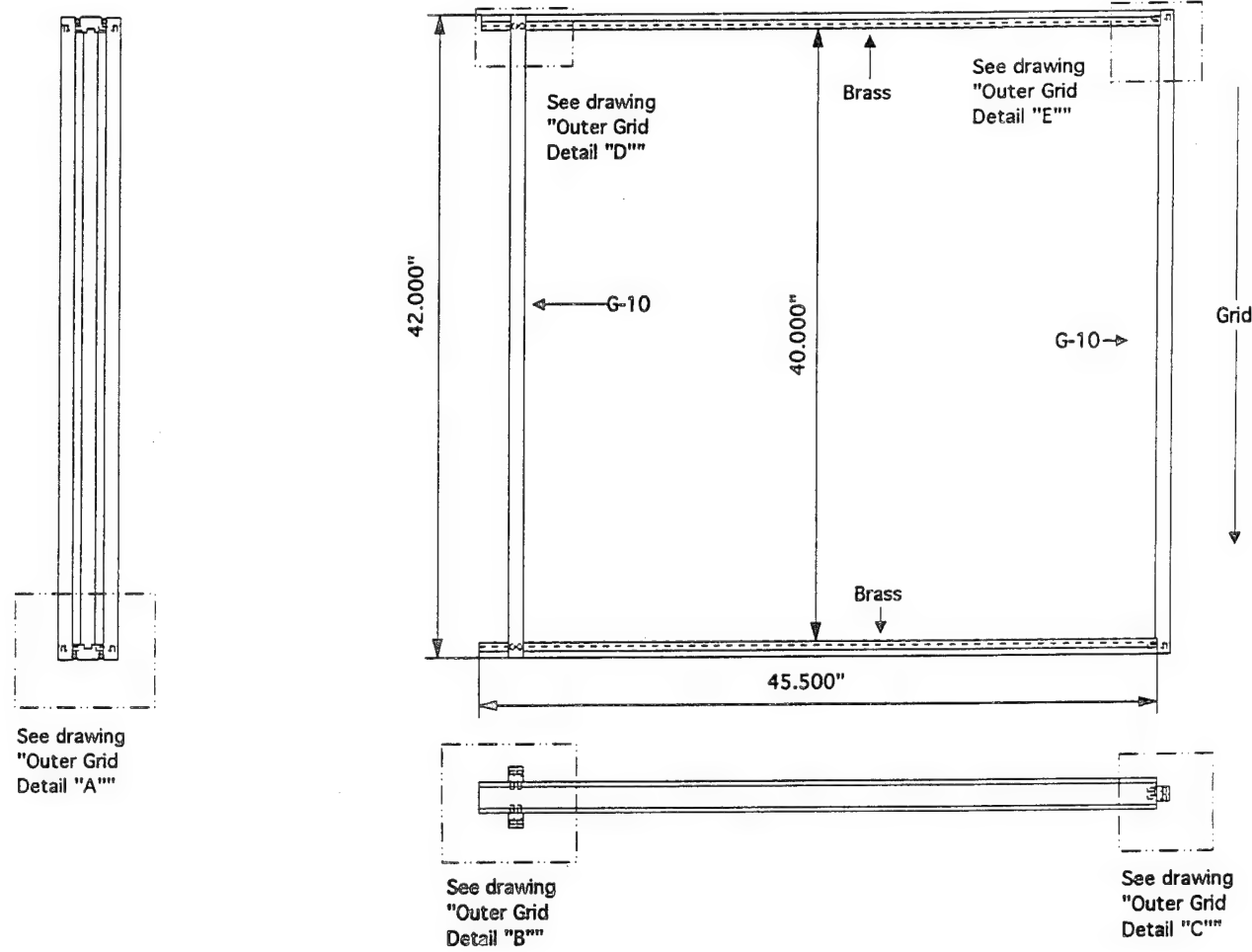


Figure (18)

Outer Grid I

Outer Grid
Detail "A"

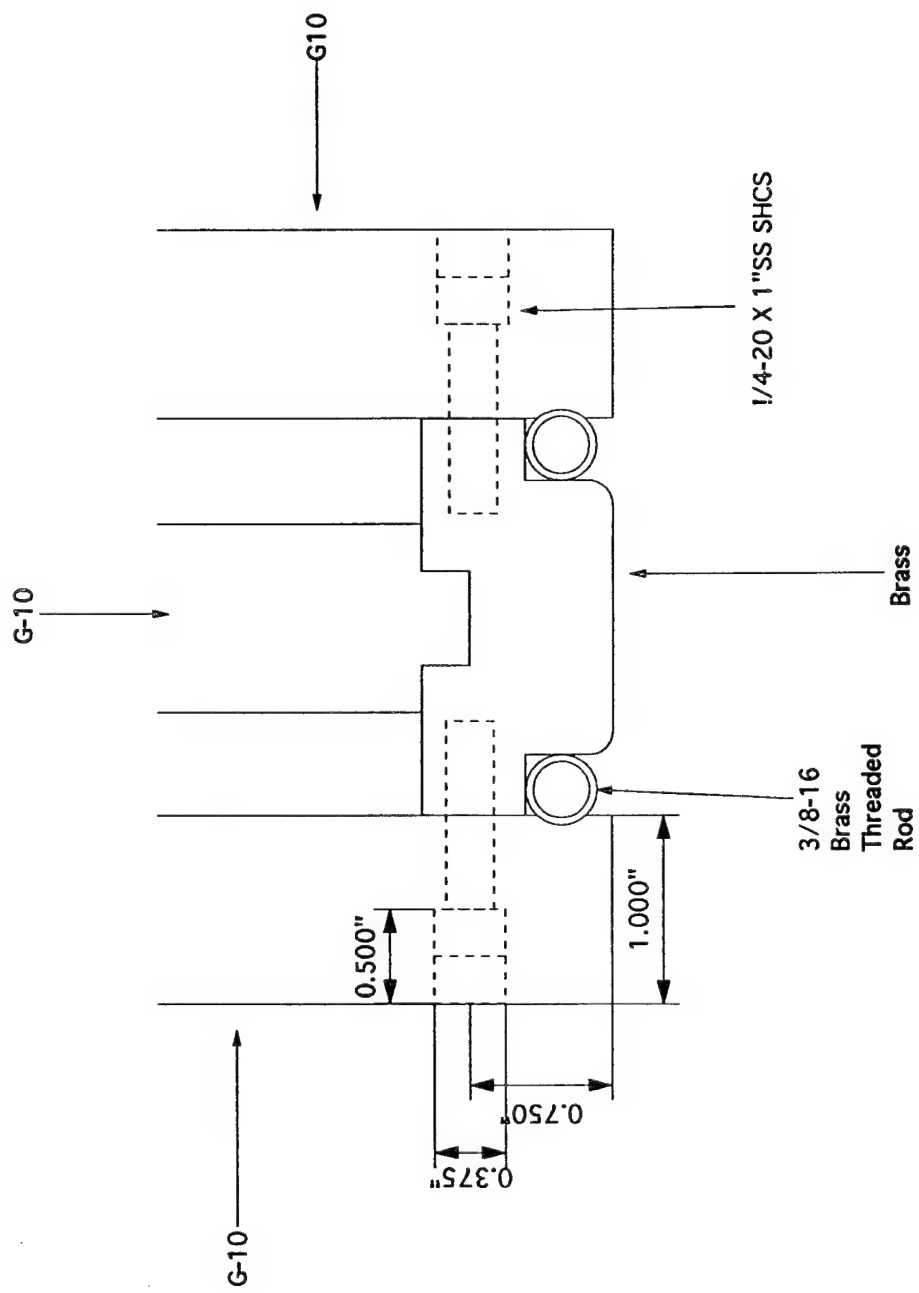


Figure (19)

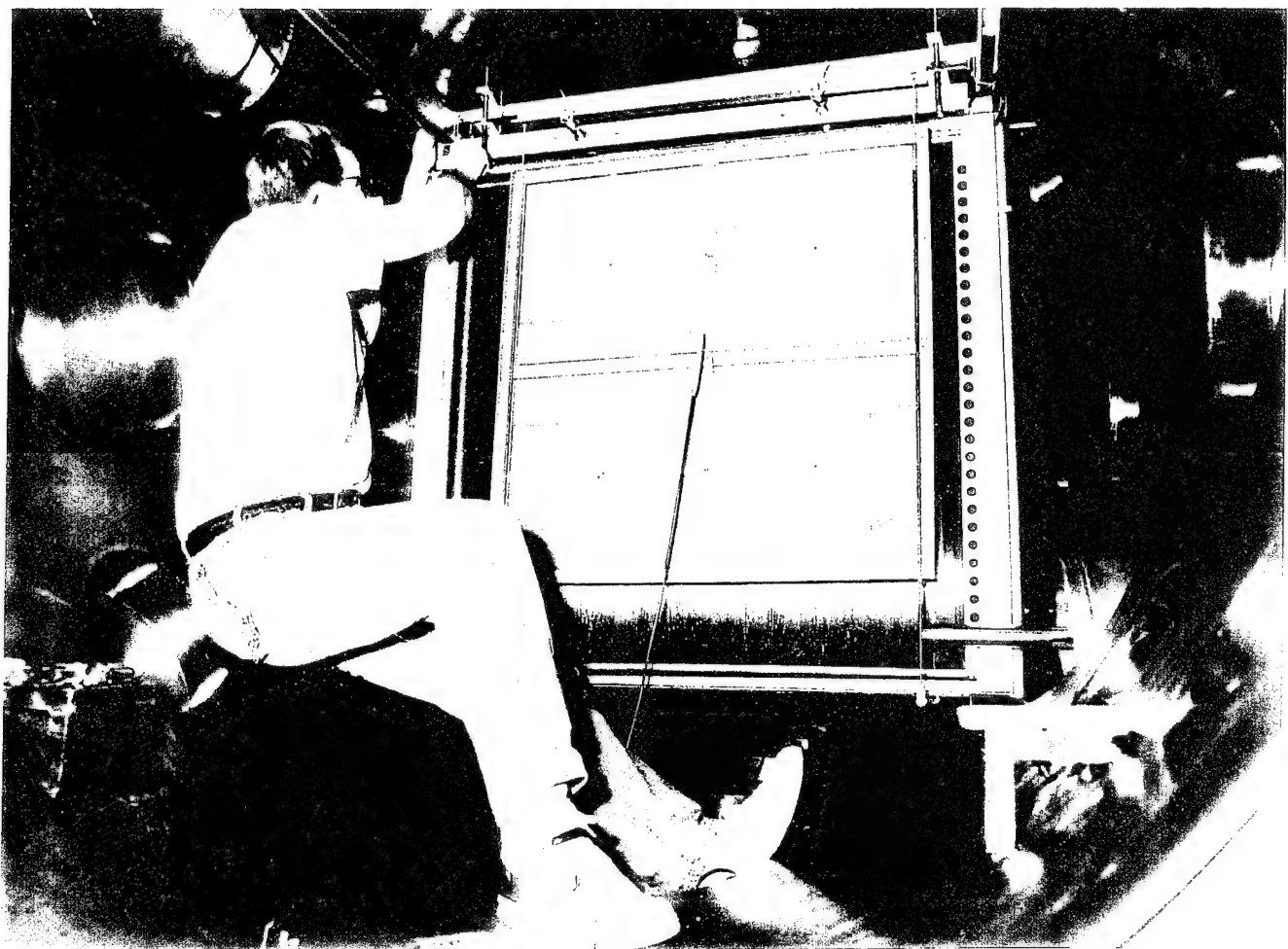
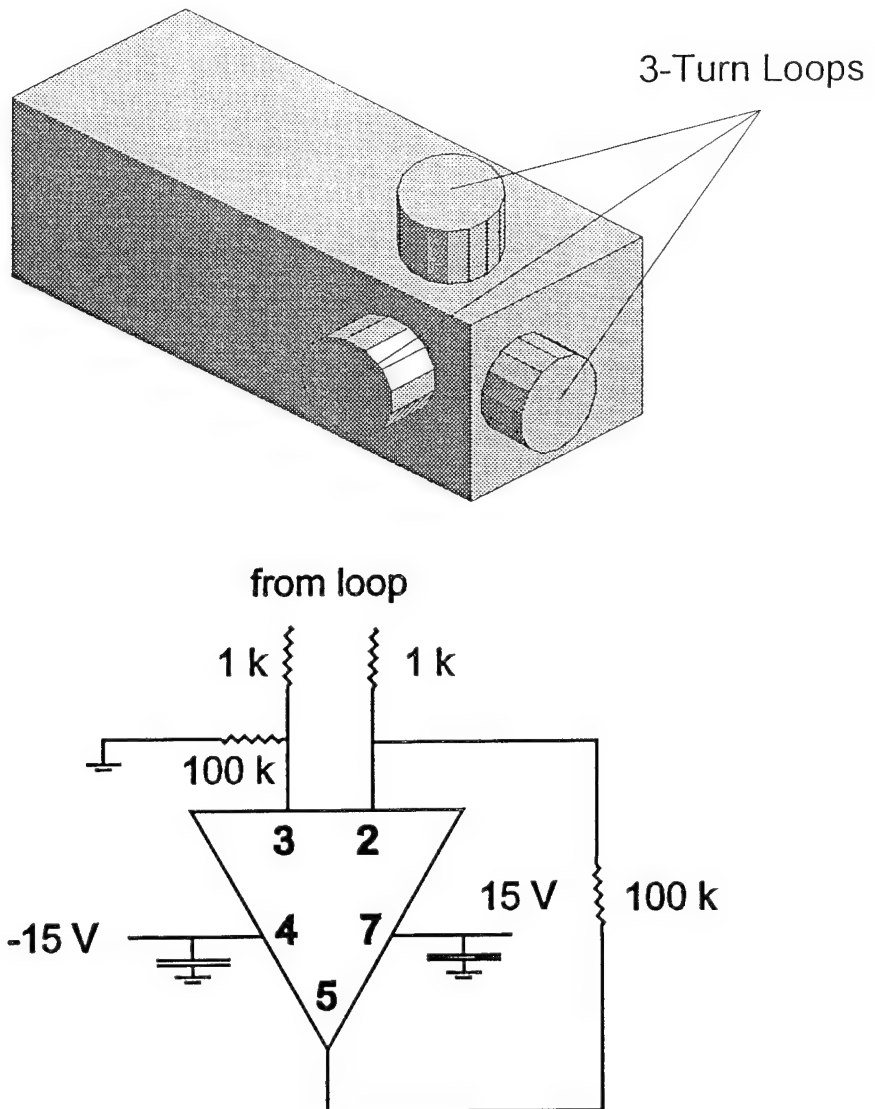


Figure (20)

3 Axis B-dot Probe



Op Amp is Burr Brown
opa 620
All resistors 1%

Figure (21)

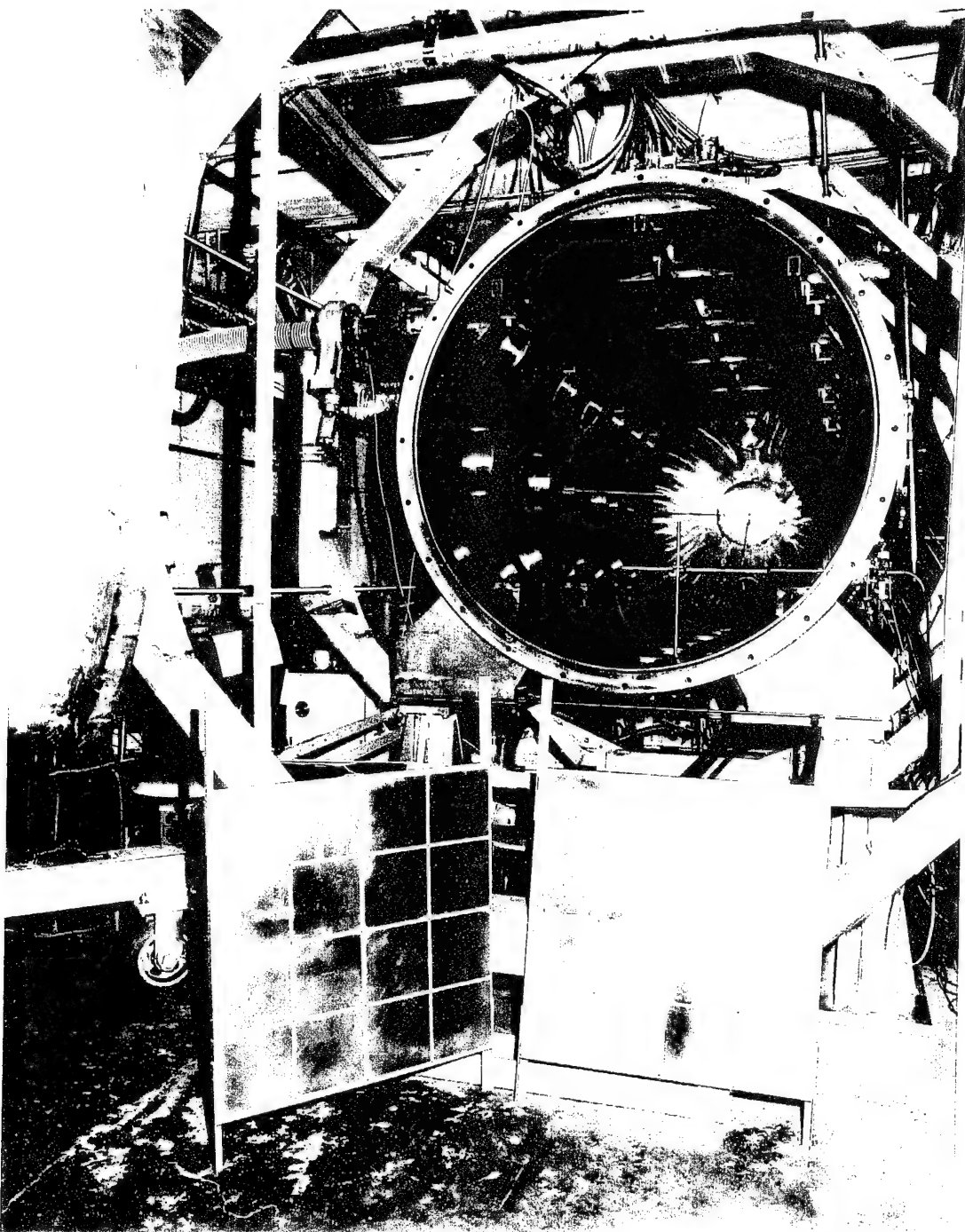


Figure (22)

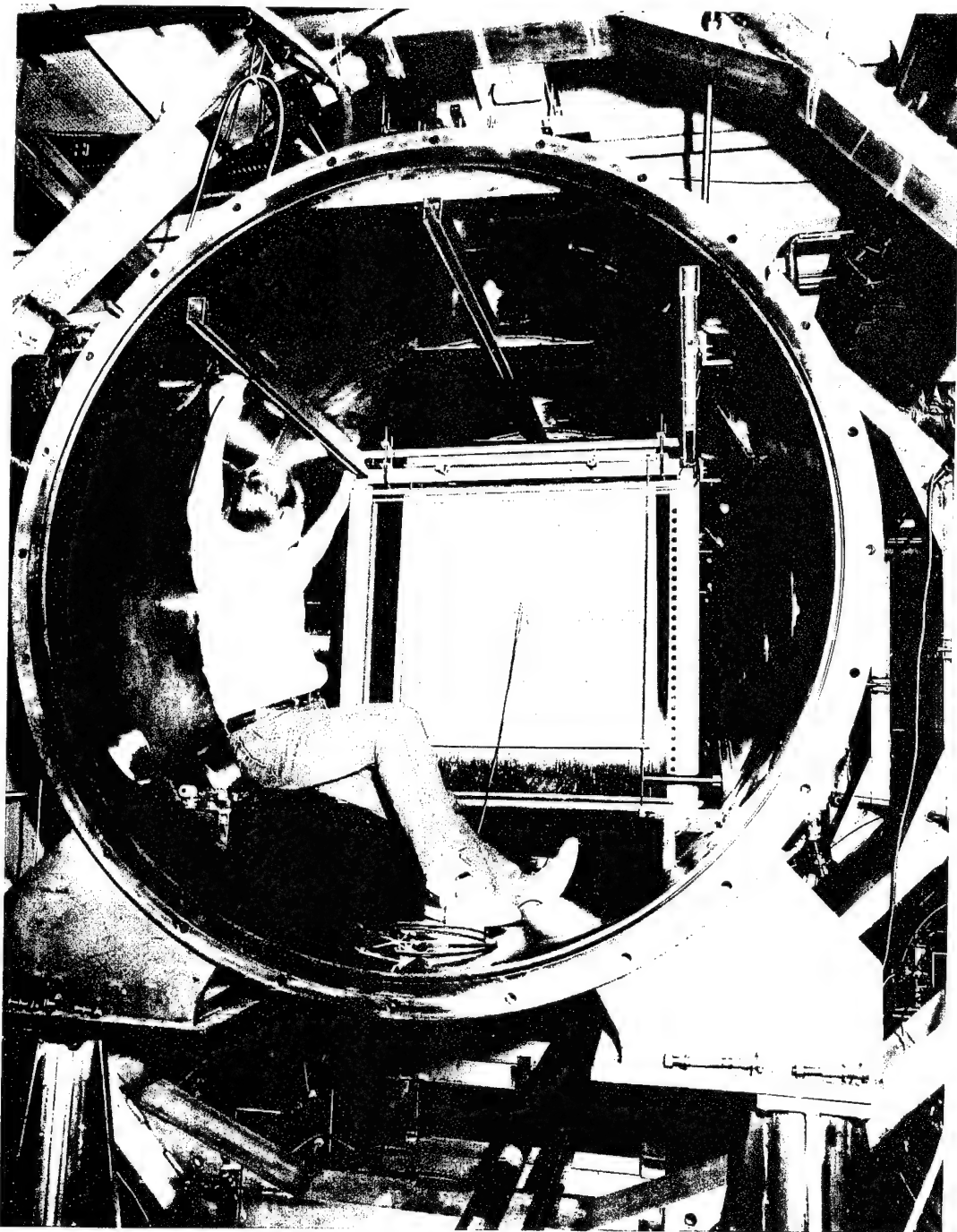


Figure (23)

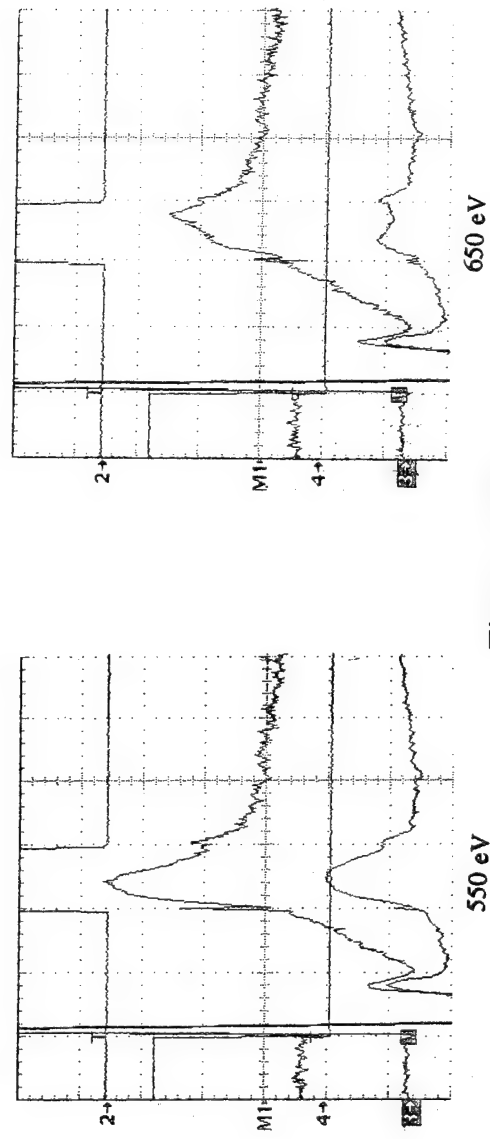
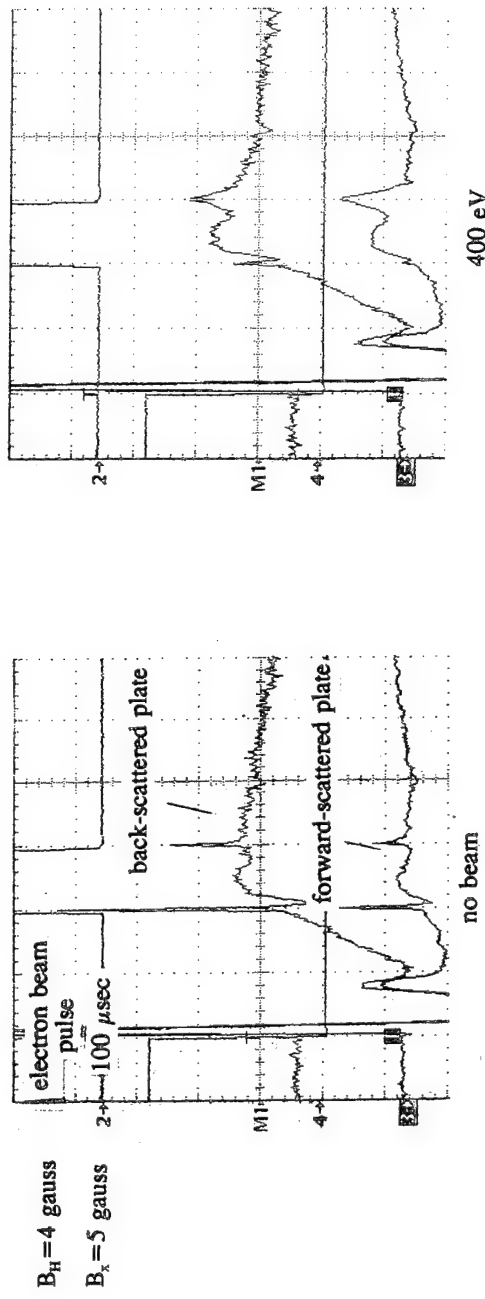


Figure (24)

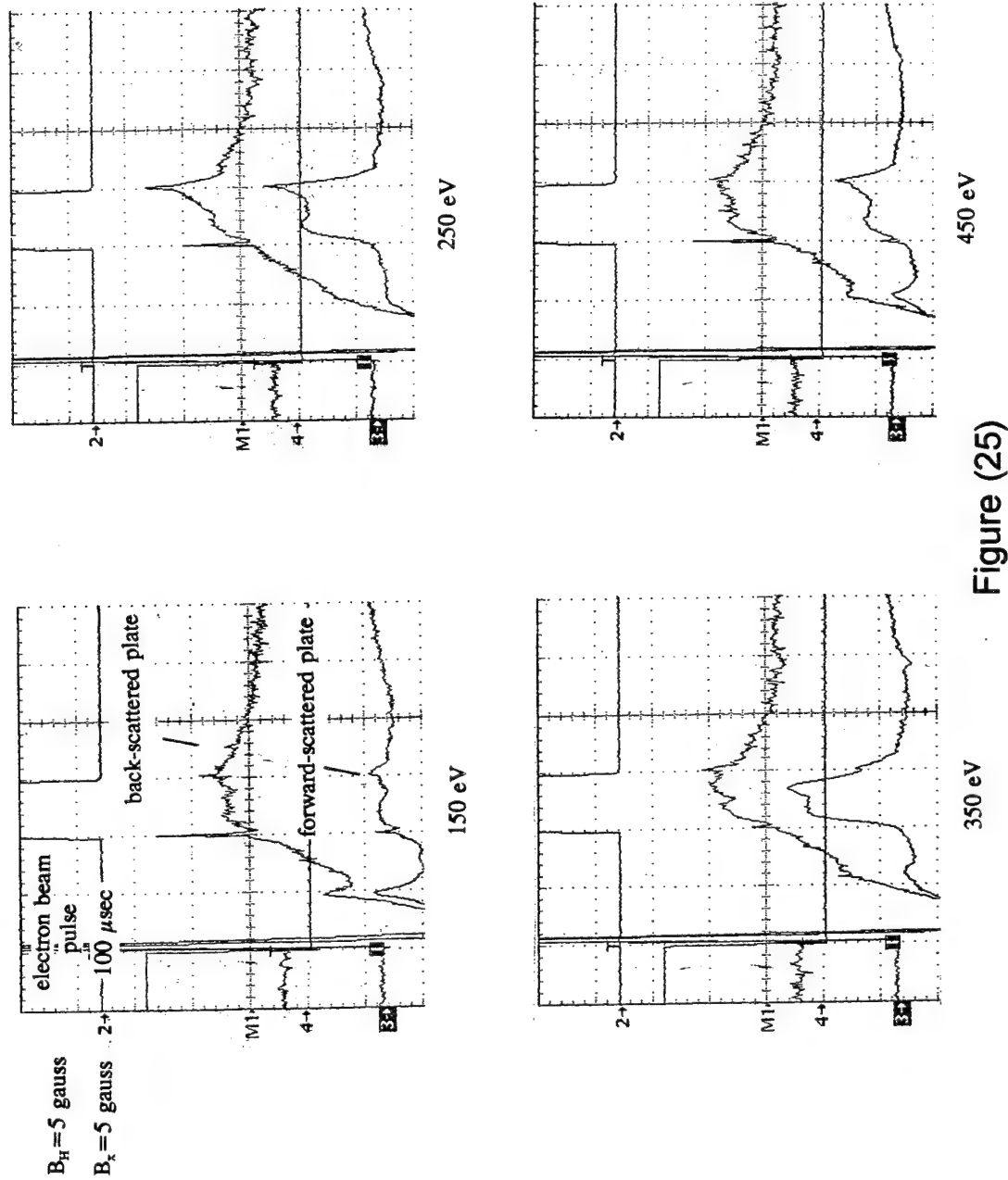


Figure (25)

PULSE FORMING NETWORK FOR B FIELD GRIDS
USED IN CHAOS EXPERIMENT

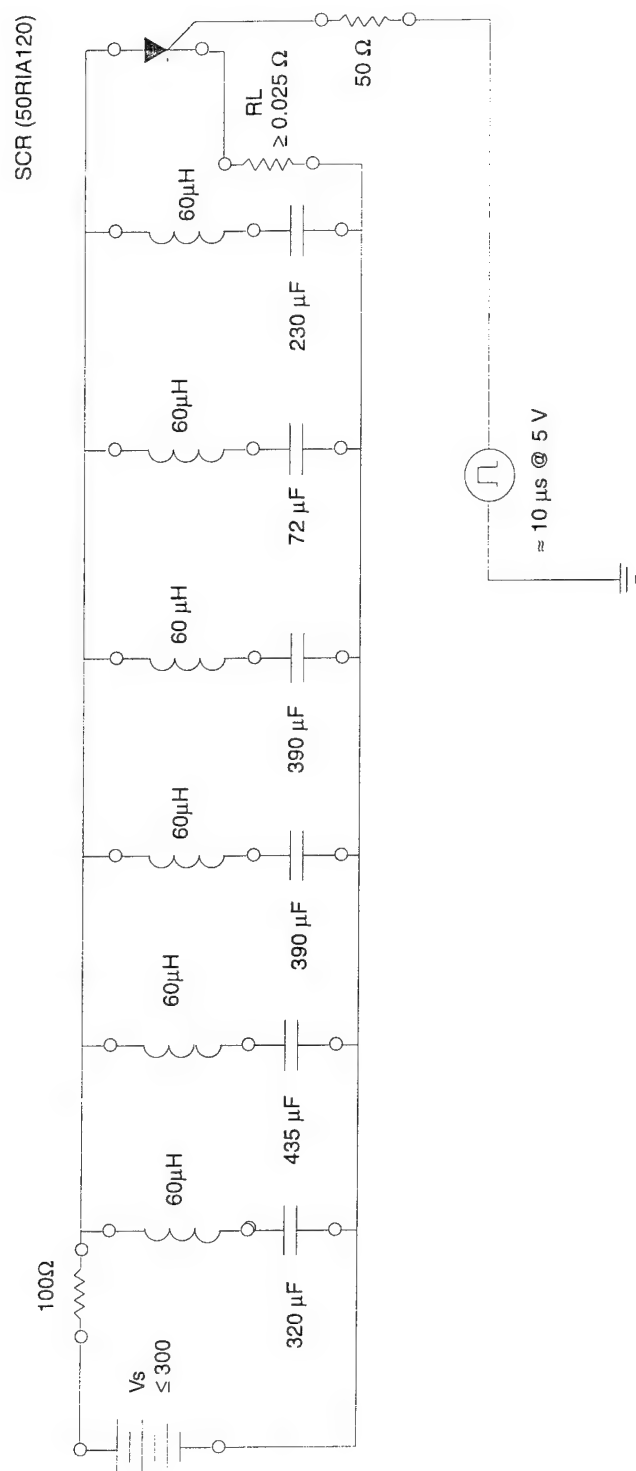


Figure (26)

Dwight Duncan
4/12/93



Figure (27)

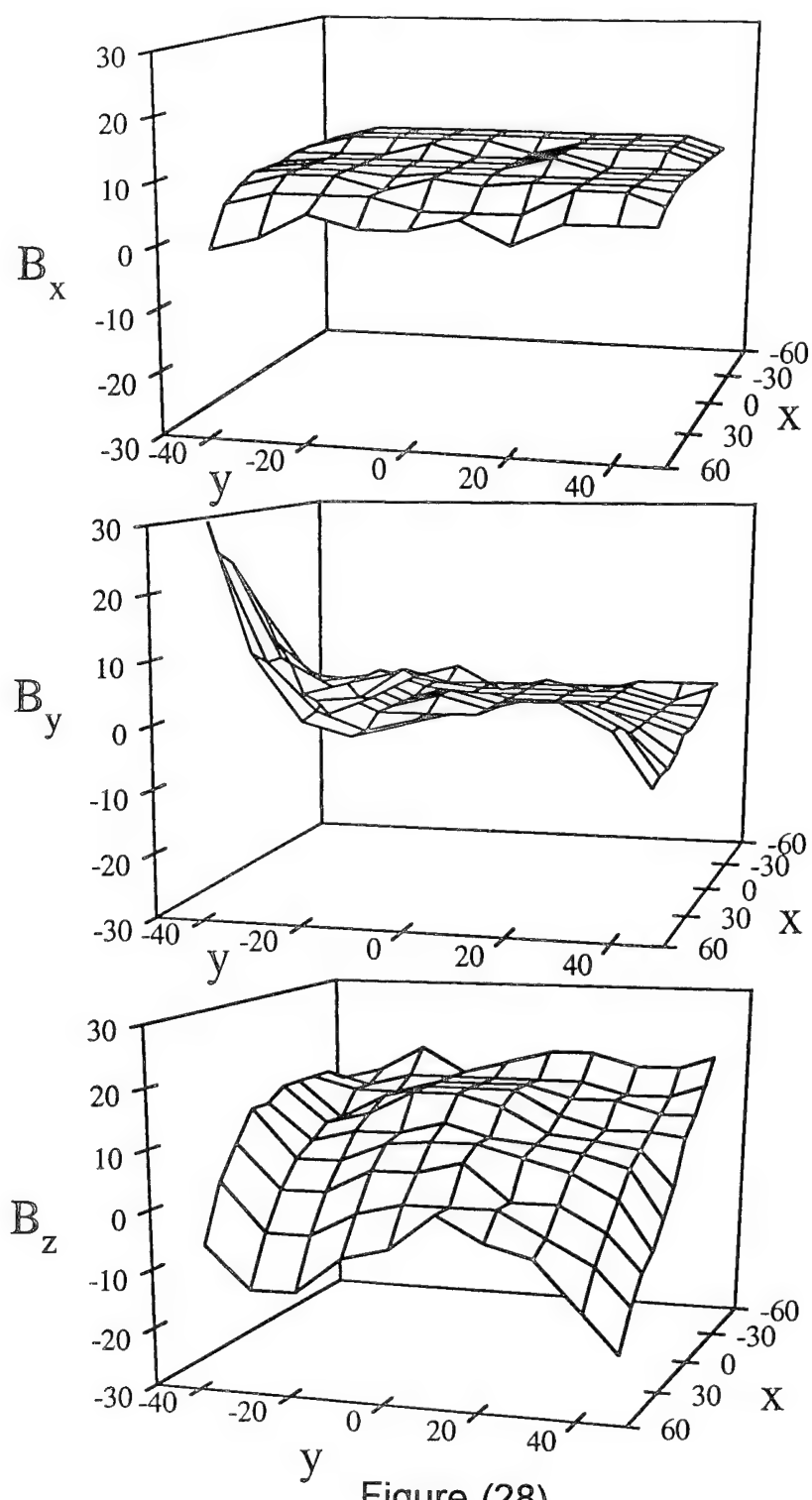


Figure (28)

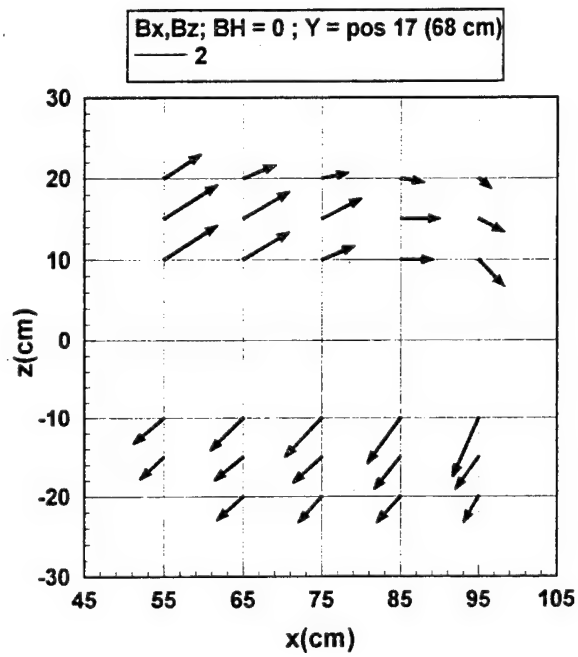
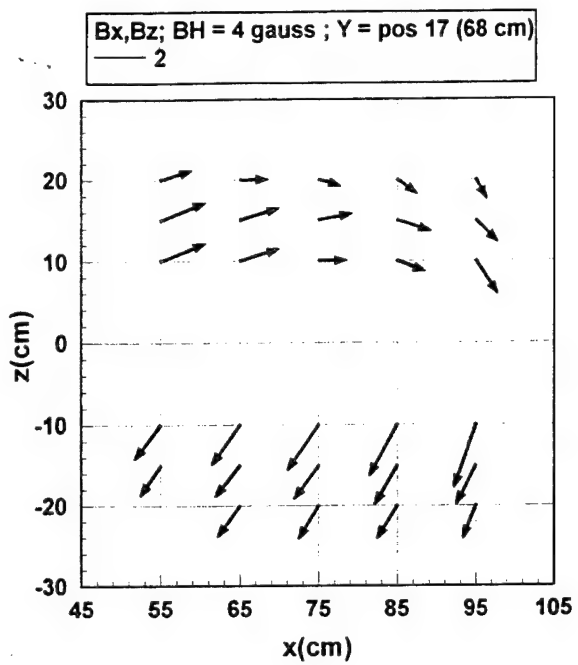
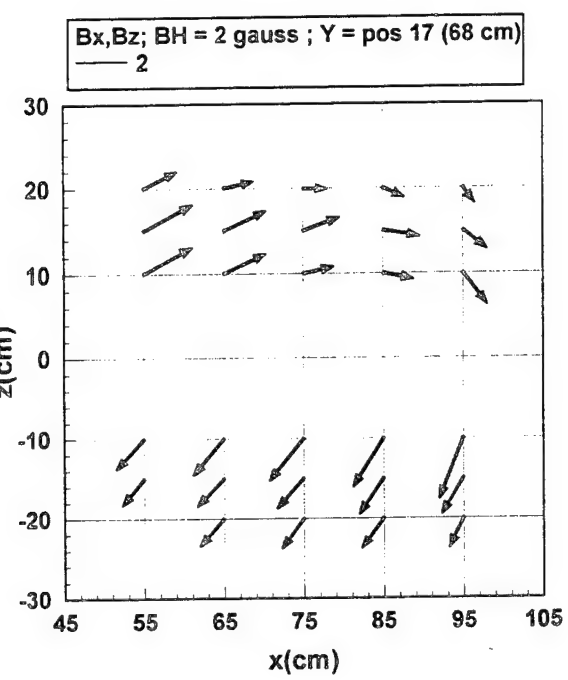


Figure (29)



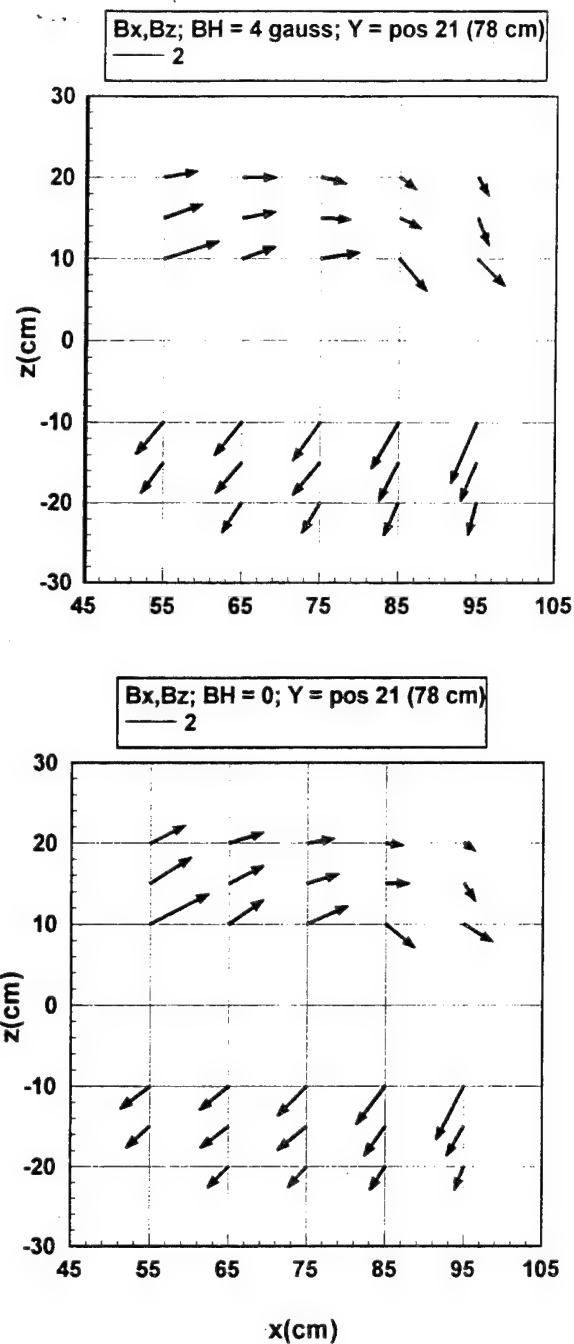


Figure (30)

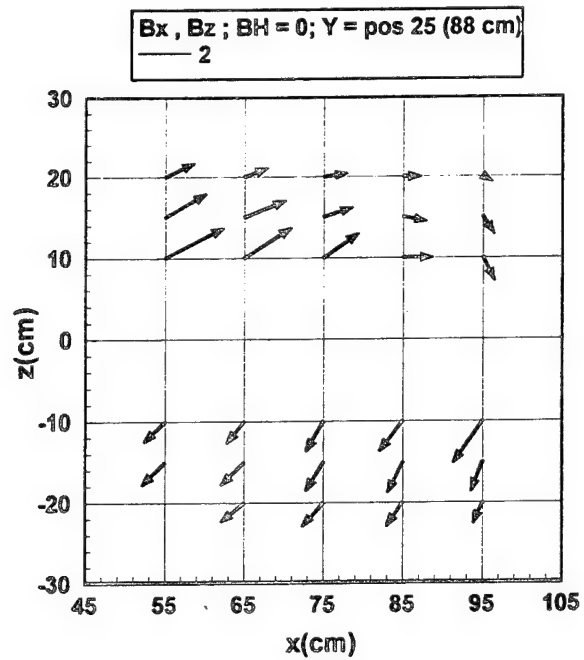
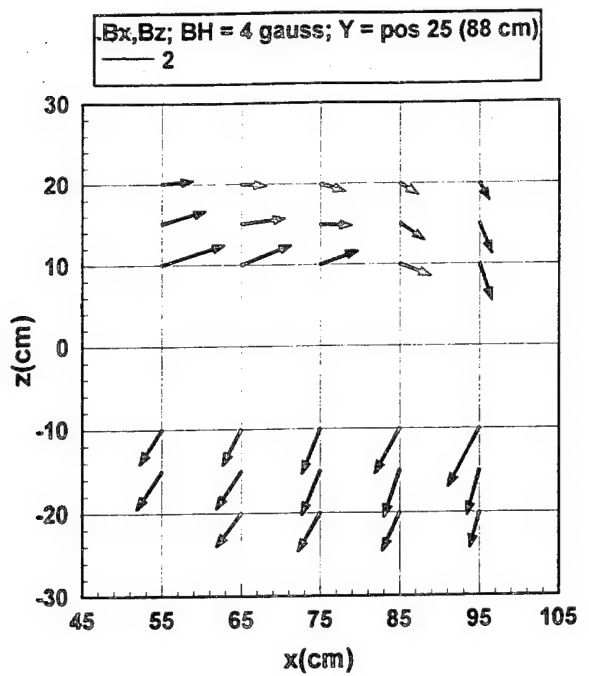


Figure (31)

B MMT - B(DOT) LOOPS-XZ PLANE

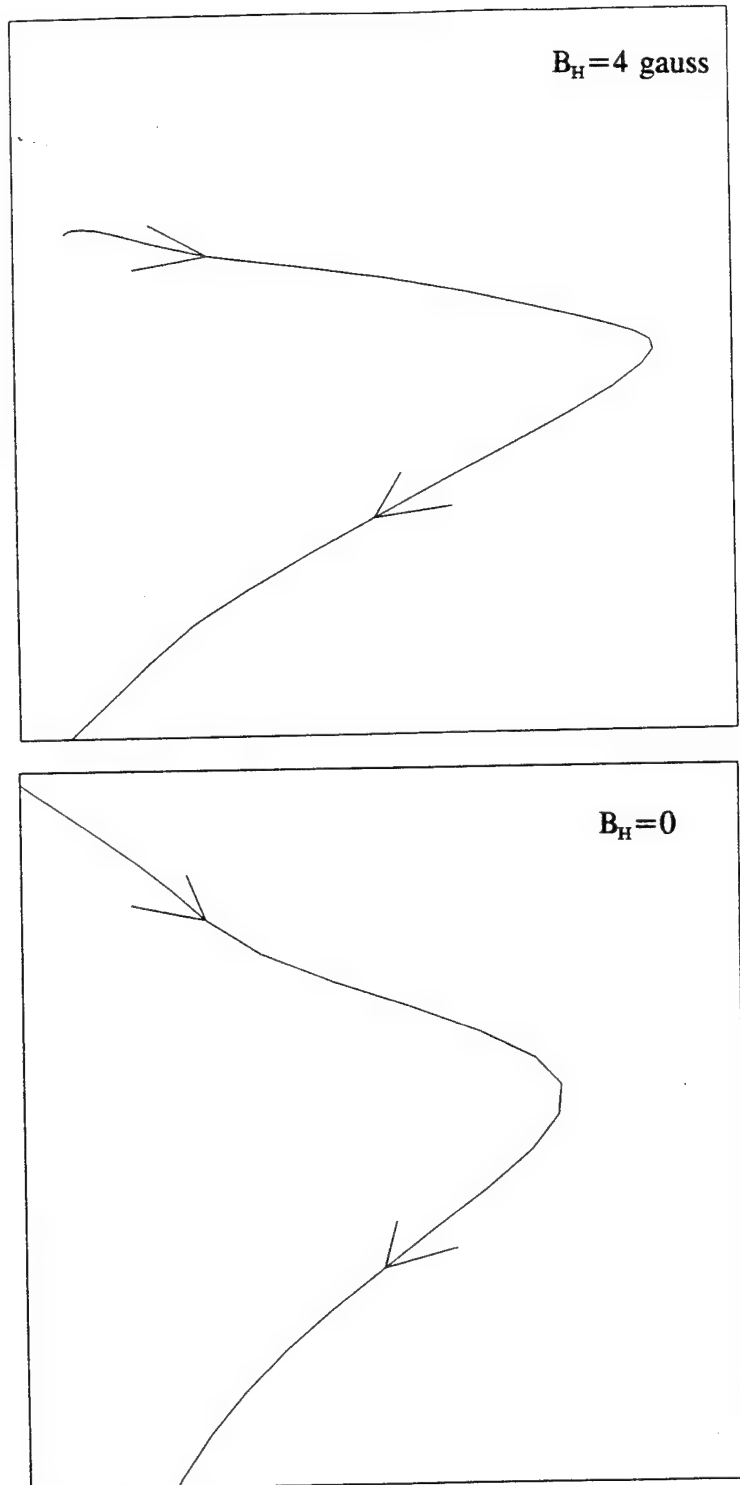


Figure (32)

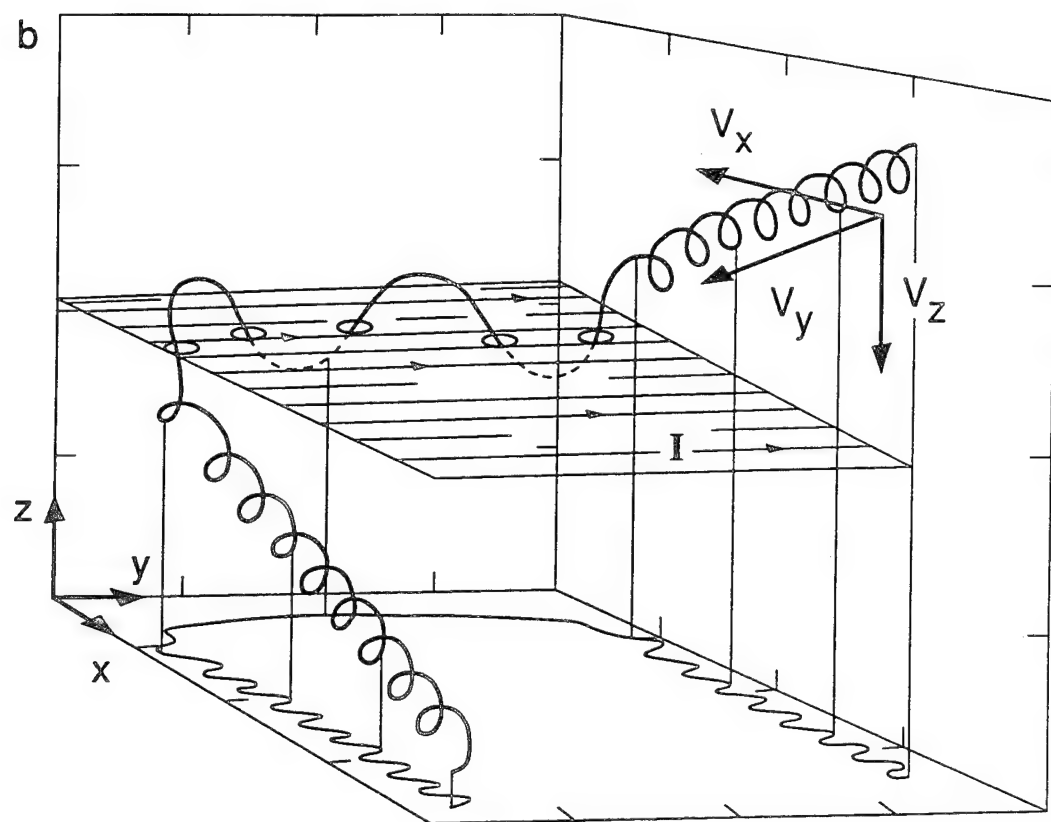


Figure (33)

Z-Y PLANE PROJECTION OF INJECTION
VELOCITY NORMAL TO \mathbf{B}

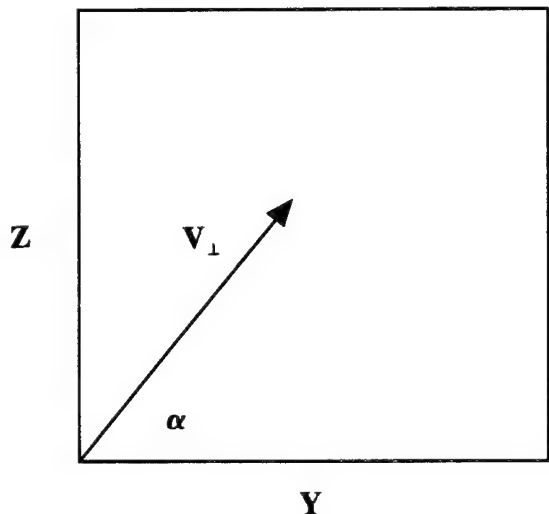
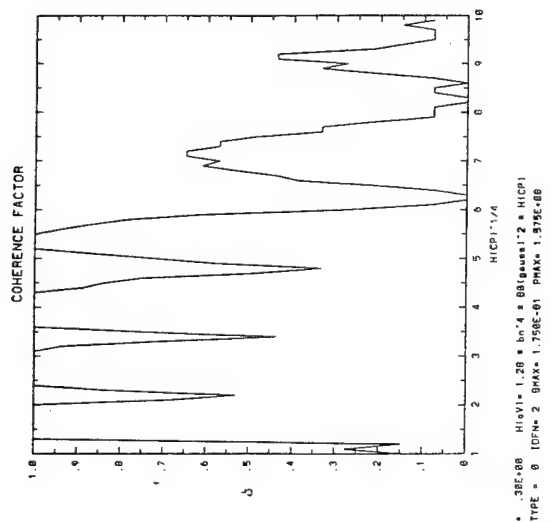
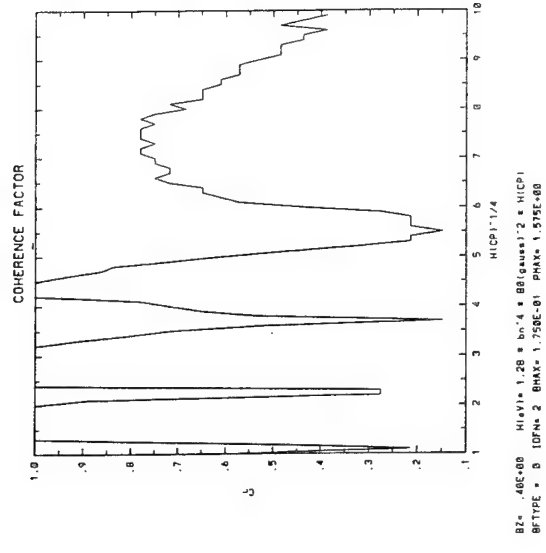


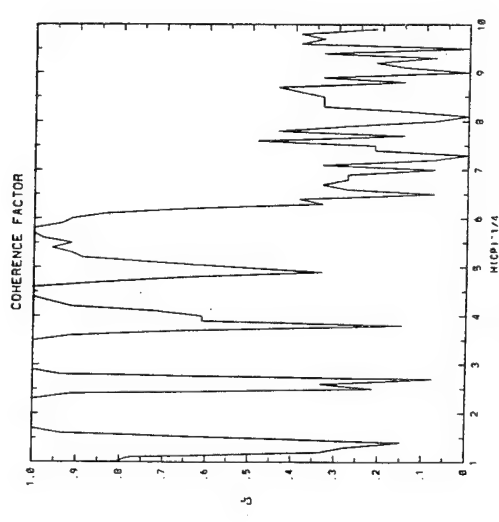
Figure (34)



(a)



(c)

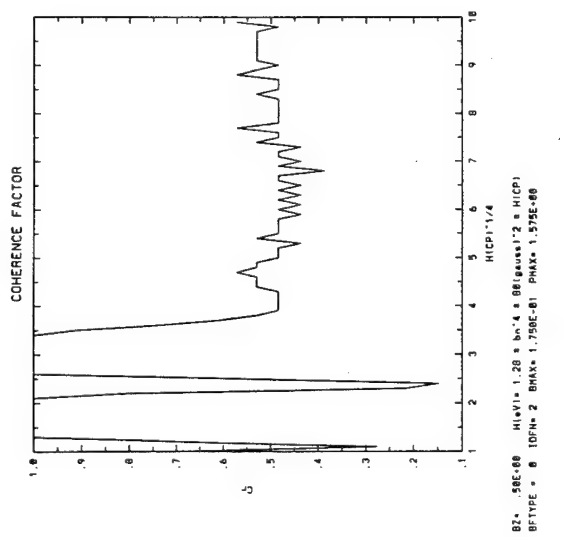


(b)

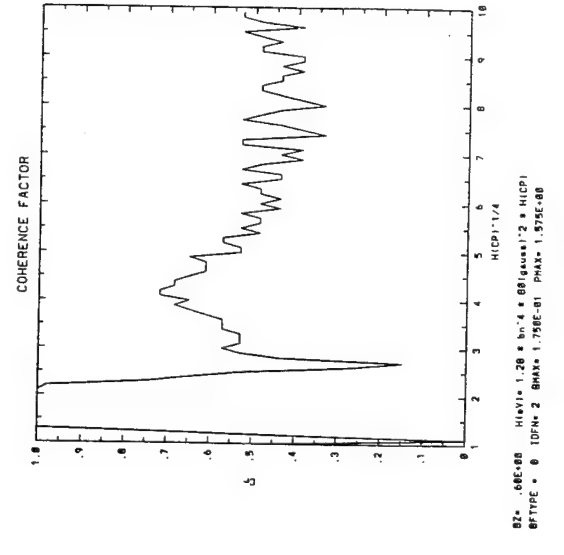
Figure (35)



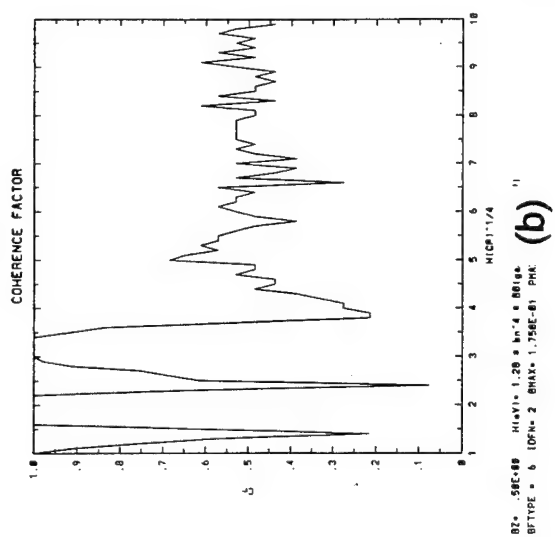
(d)



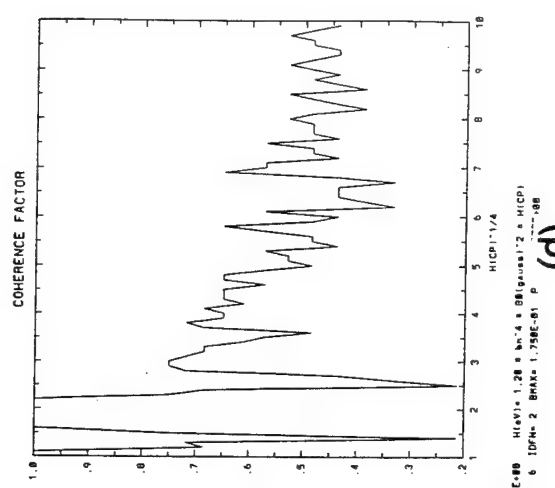
(a)



(c)



(b)



(d)

Figure (36)

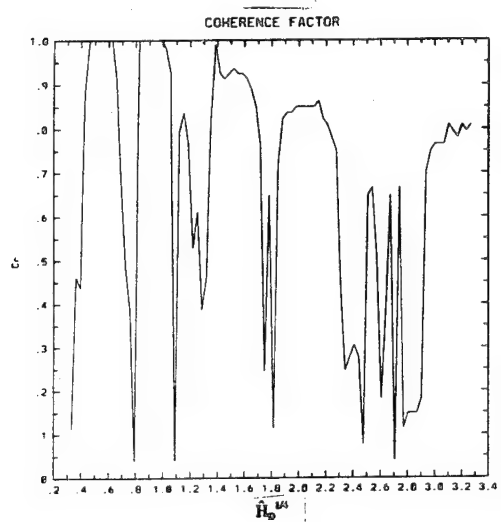
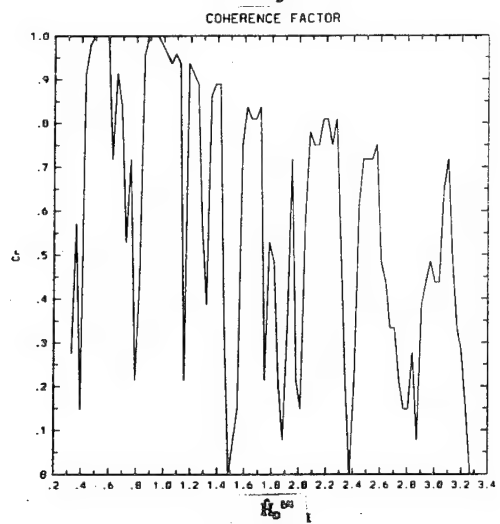
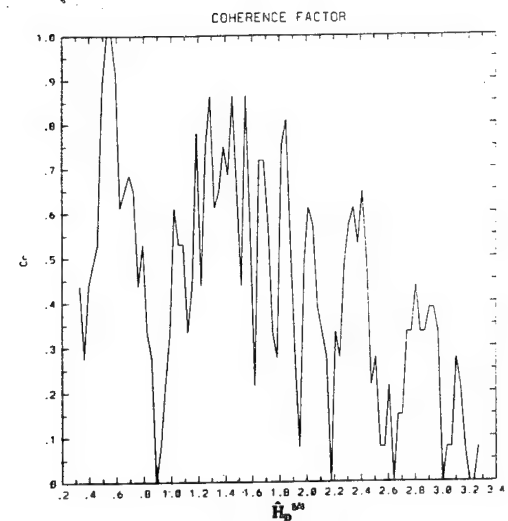


Figure (37)

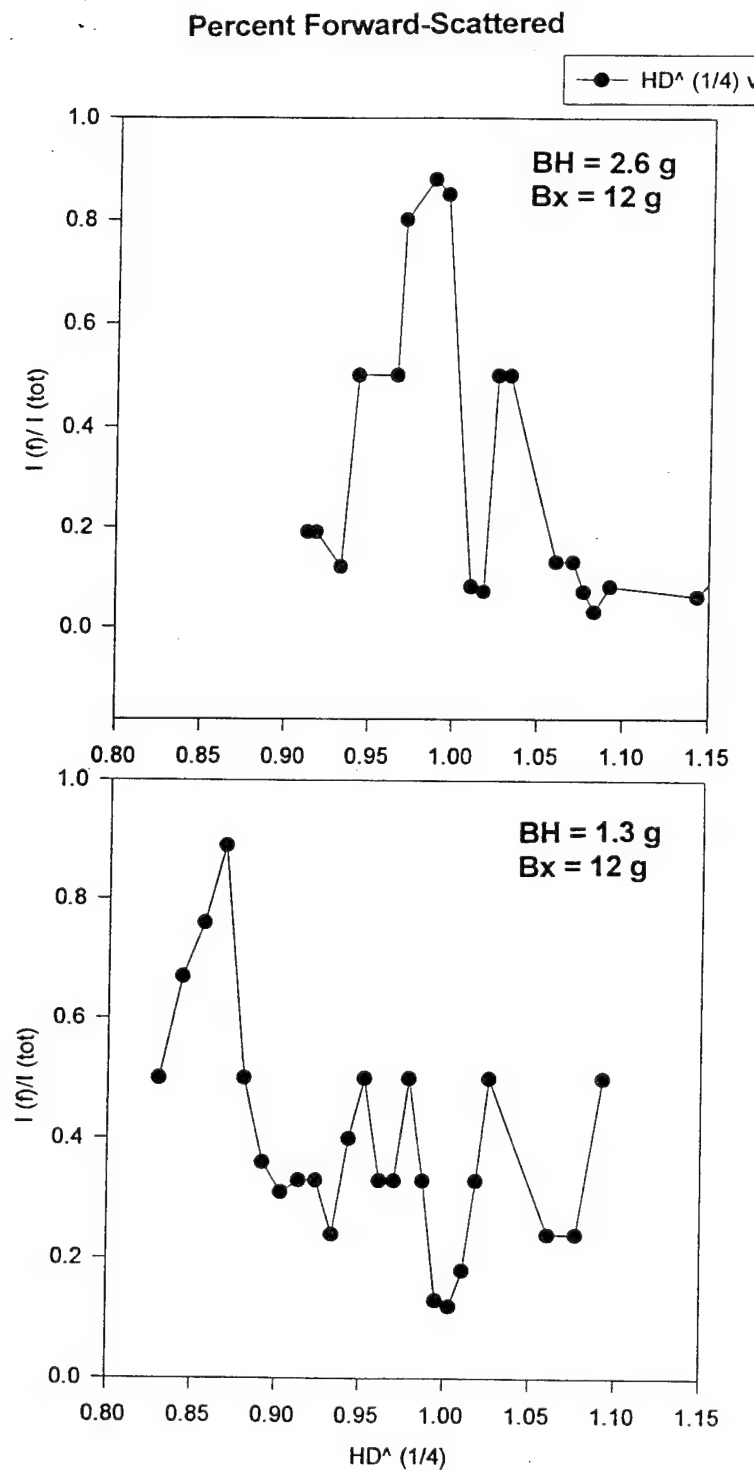


Figure (38)

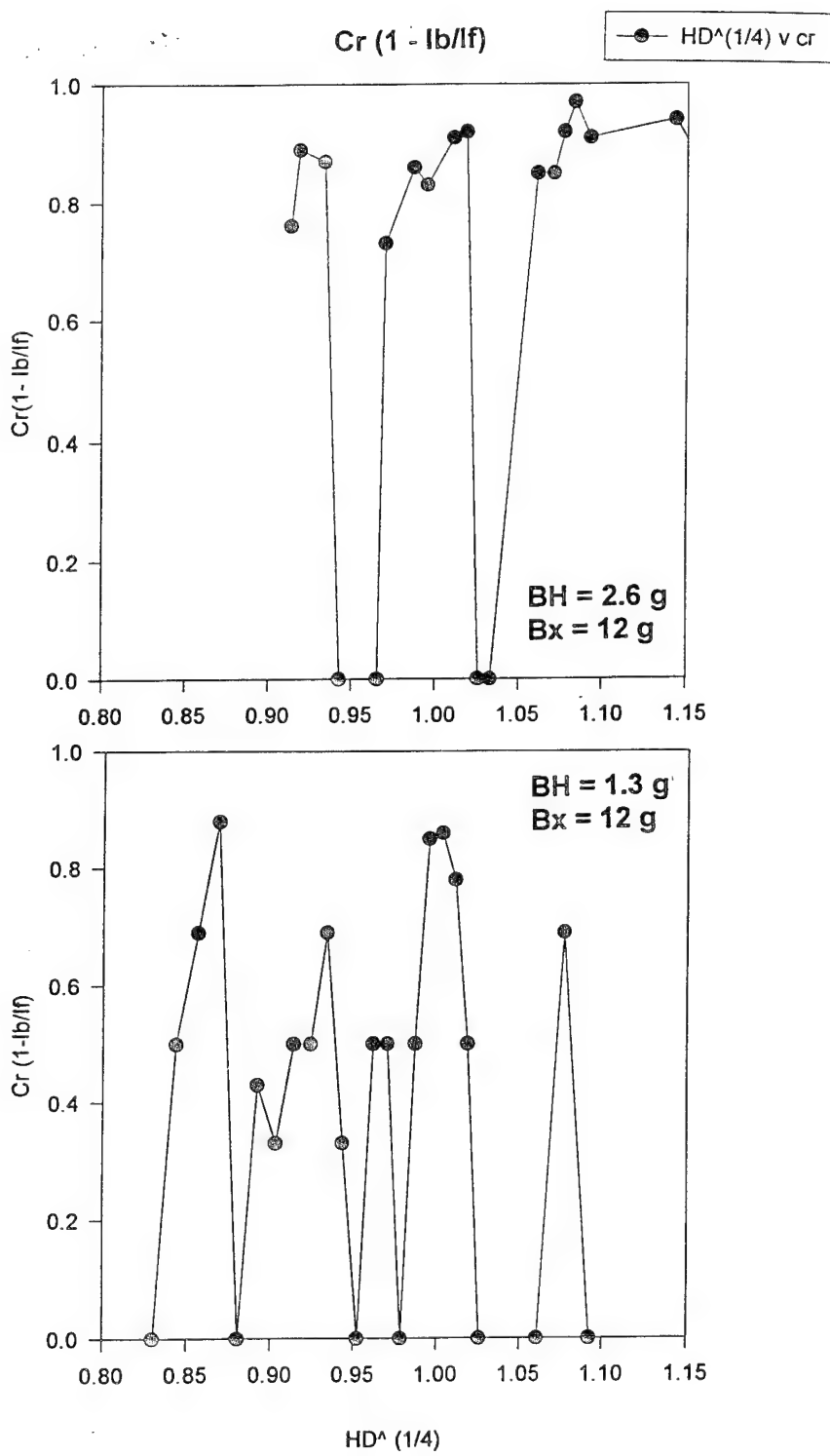


Figure (39)

Cr vs $H^{\wedge}(1/4)$ 9-MAR-95

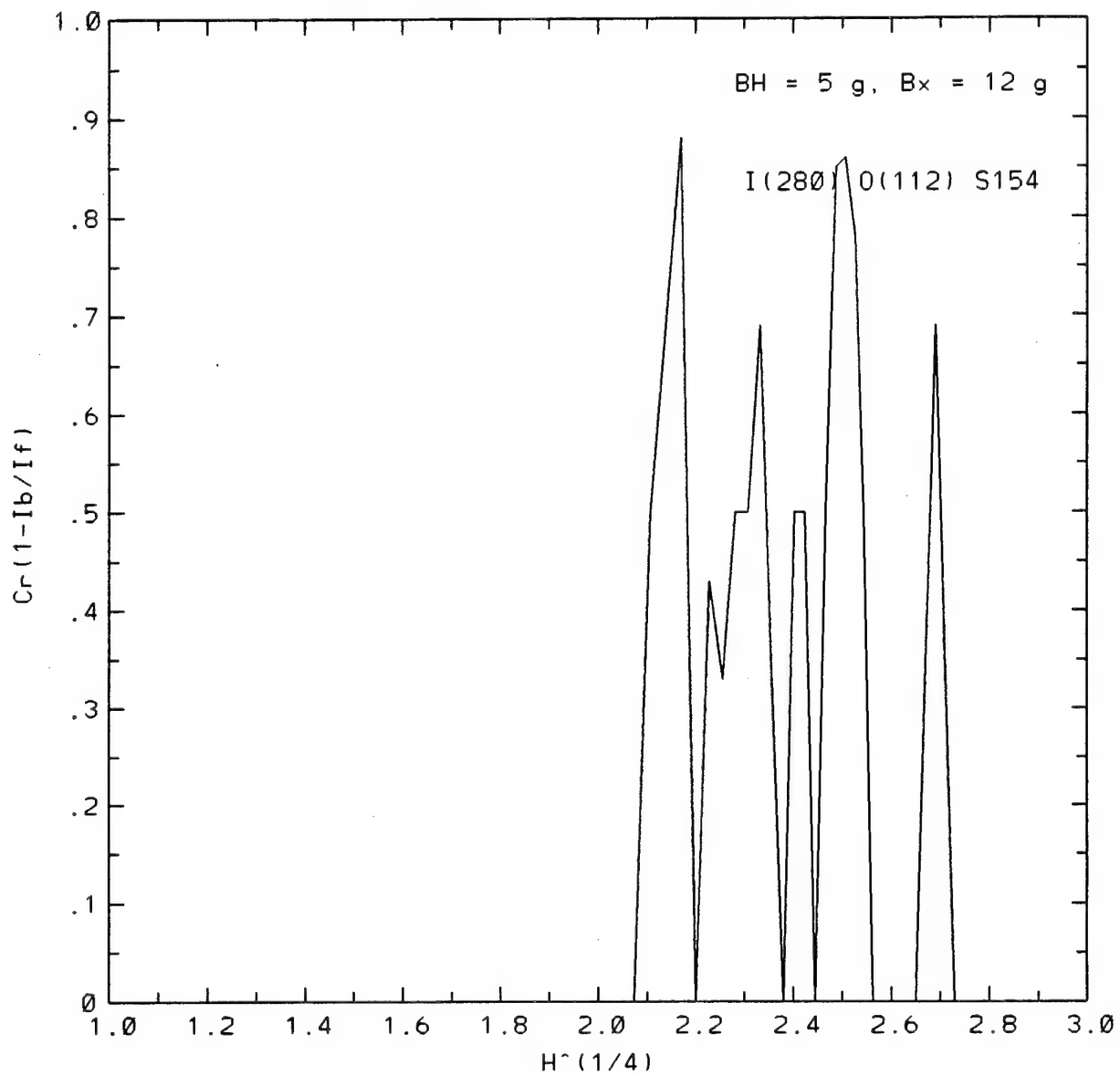


Figure (40)

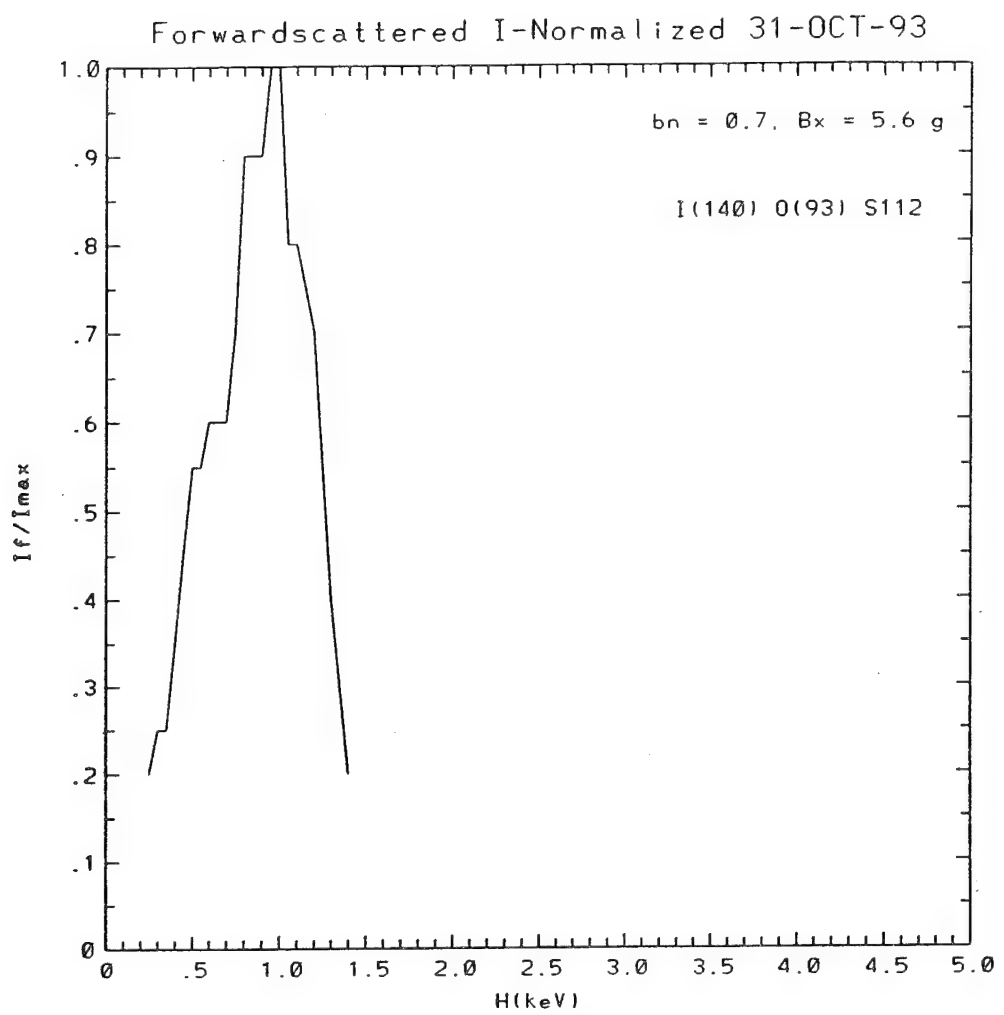


Figure (41)

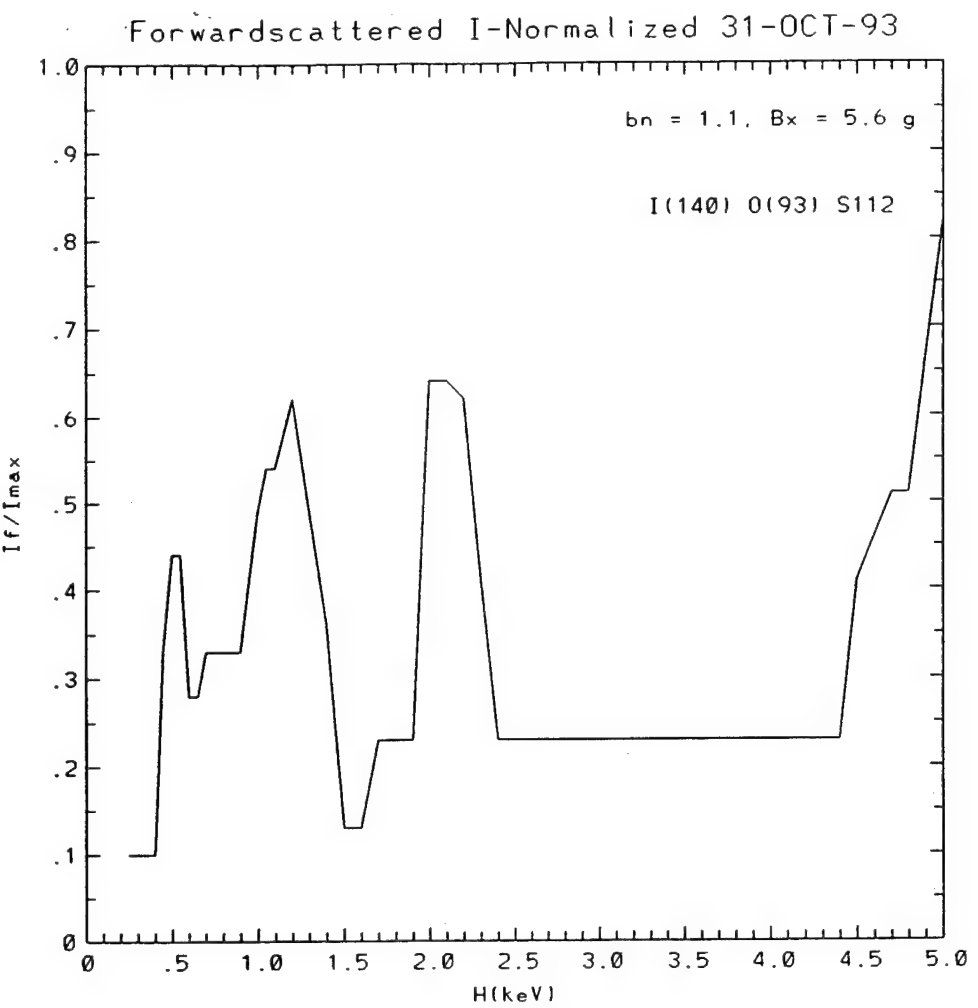


Figure (42)

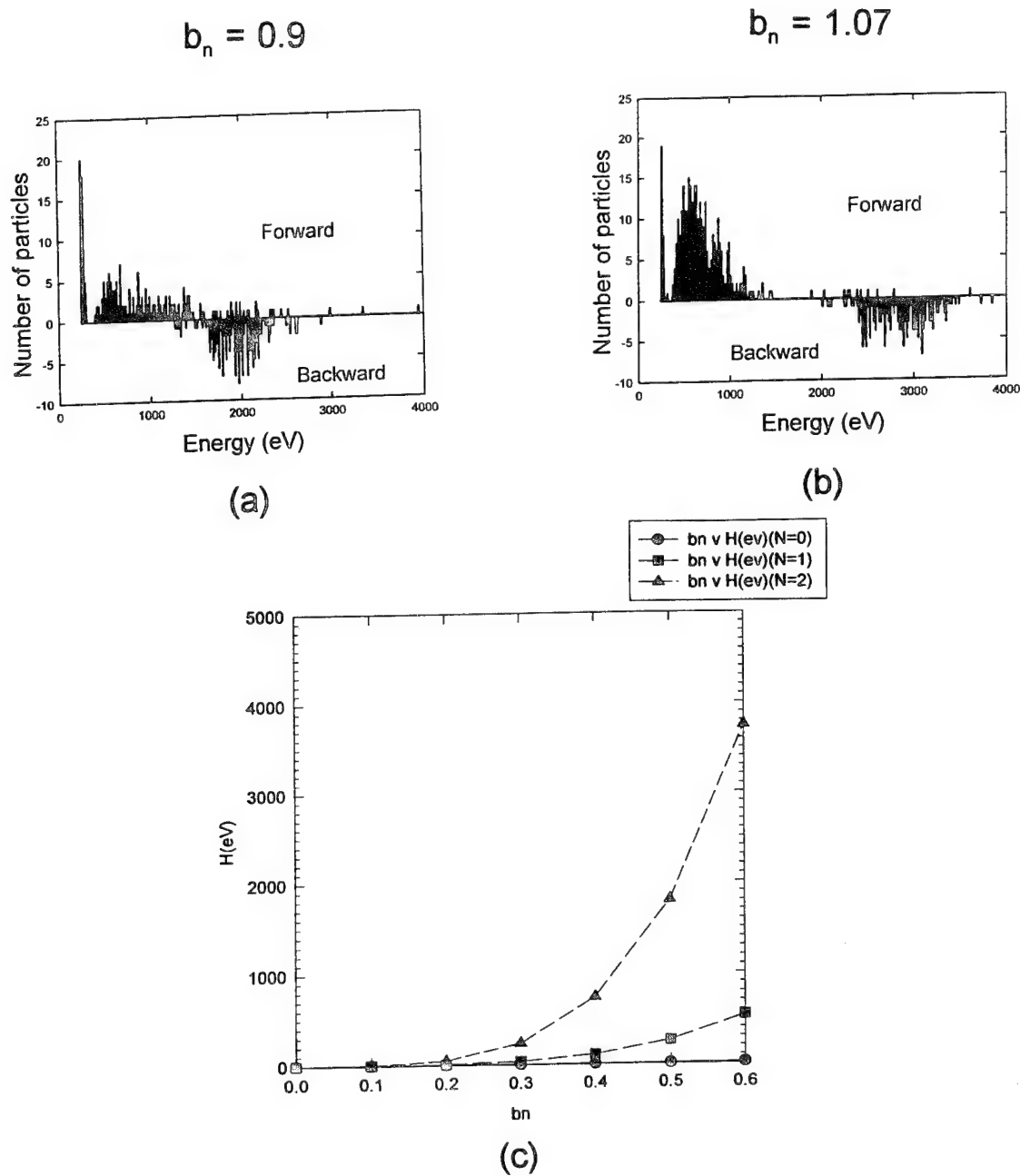


Figure (43)

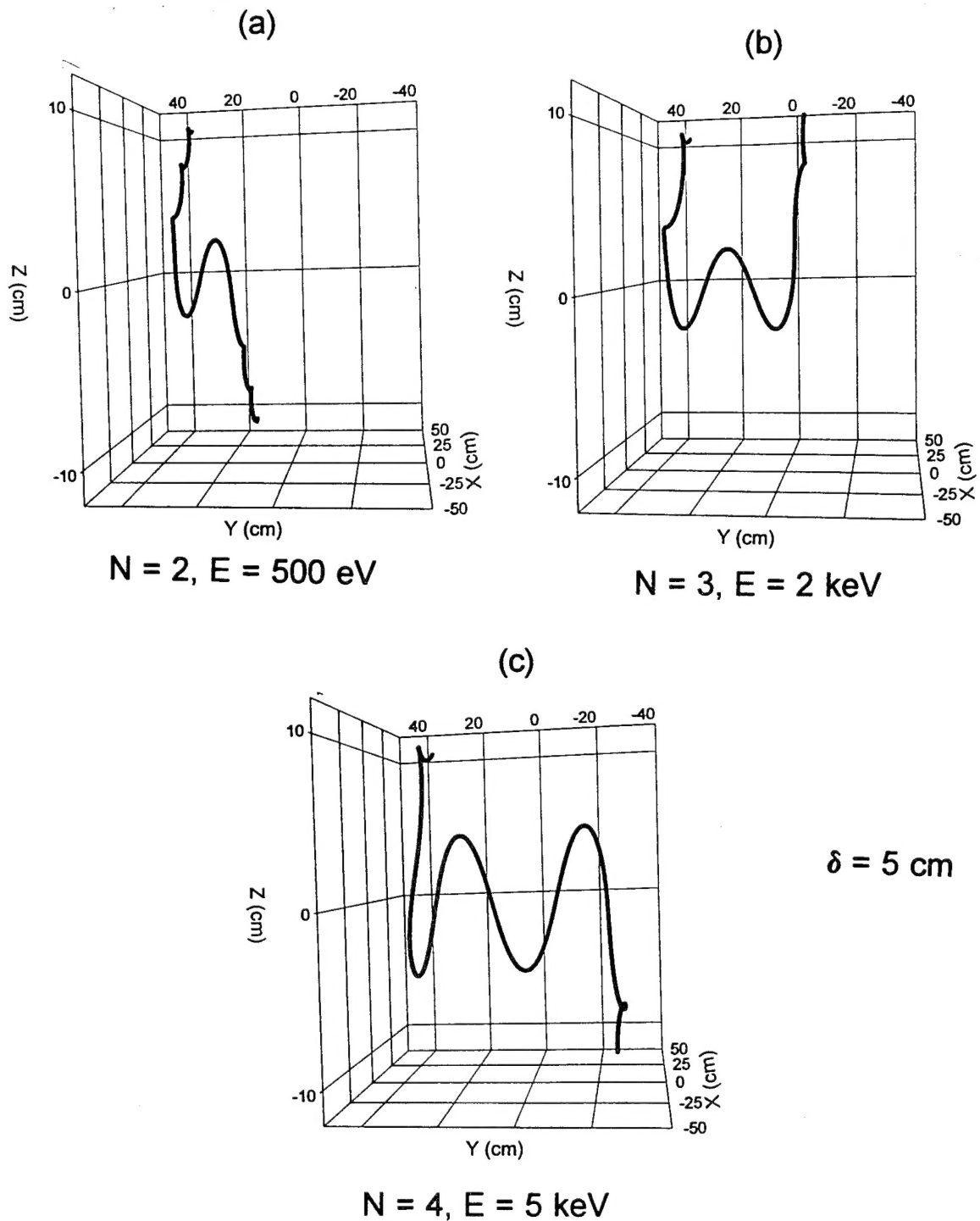


Figure (44)

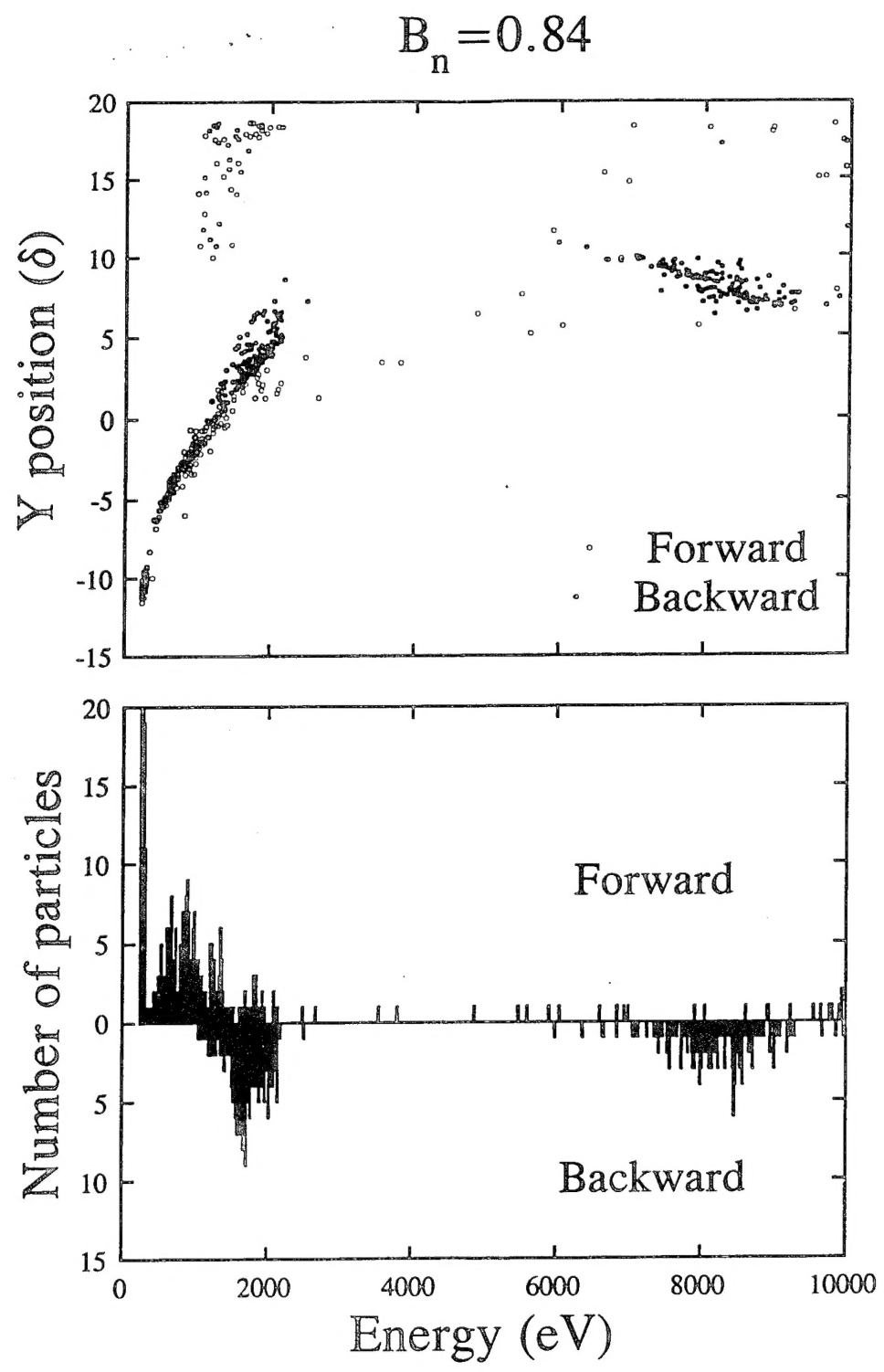


Figure (45)

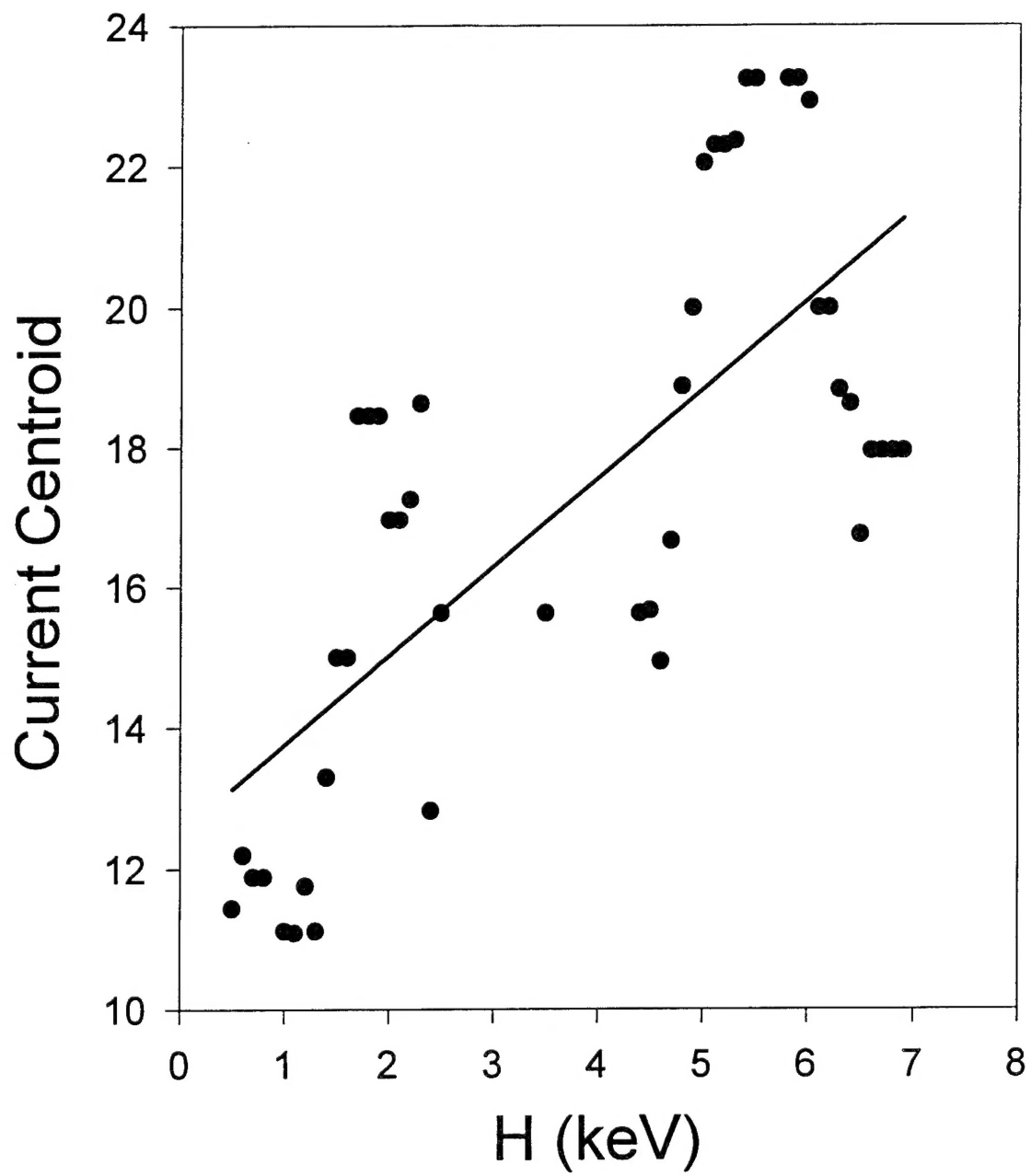


Figure (46)

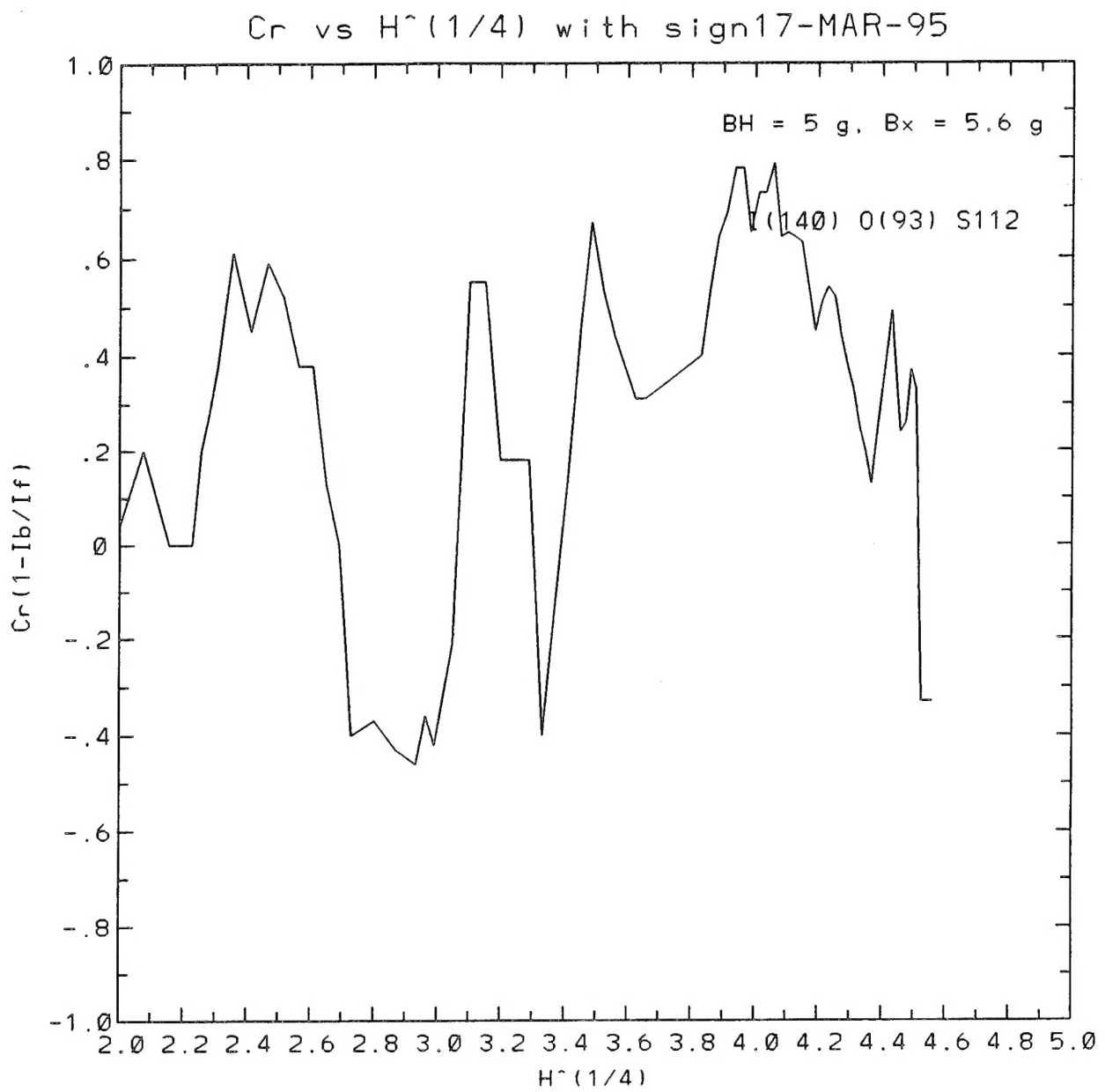


Figure (47)